Analysis of energy conversion capability among various magnetostrictive materials for energy harvesting

Yuanyuan Liu, Mickael Lallart, Benjamin Ducharne, Kanjuro Makihara, Gael Sebald

Analysis of energy conversion capability among various magnetostrictive materials for energy harvesting

Yuanyuan Liu [1,2,3,*], Mickael Lallart [1], Benjamin Ducharne [3], Kanjuro Makihara [2] and Gael Sebald[3,*]

1 University Lyon, INSA-Lyon, LGEF EA682, F-69621 Villeurbanne, France

2 Department of Aerospace Engineering, Tohoku University, Sendai 980-8579, Japan

3 ELyTMaX UMI 3757, CNRS, University Lyon, INSA Lyon, Centrale Lyon, Université Claude Bernard Lyon 1, Tohoku University, Sendai 980-8579, Japan

* Correspondence: gael.sebald@insa-lyon.fr; yuanyuan.liu@insa-lyon.fr

Abstract

This work addresses vibrational energy harvesting using magnetostrictive materials. In this field, materials with exceptional magneto-mechanical coupling properties (e.g., Galfenol, Terfenol-D) have attracted significant attention. Only a few magnetostrictive materials have been tested in devices, however, leaving the actual influence of these materials' properties on the energy harvesting device open to question. This work compares an extensive range of ferromagnetic materials through analysis of their magnetic behavior under static stress. To enable fair comparison of the materials, a model was developed to interpolate their magnetic anhysteretic curves under fixed stress of σ = ±50 MPa. The energy harvesting process was then simulated using a theoretical Ericsson thermodynamic cycle, where the area represents the energy density. This approach estimates the ultimate energy density of the materials using a fair approach, without placing conditions on the applied magnetic field. The correlation between ultimate energy density and the magnetoelastic coefficient show that highly magnetostrictive materials achieve higher ultimate energy densities, as expected. In the low field range, it is however concluded that all materials exhibit energy densities of the same order of magnitude. Secondly, the magnetoelastic coefficient versus excitation field characteristics revealed an optimal bias magnetic field for each material. Finally, for realistic implementation, the paper considers a pre-stress in combination with a bias magnetic field and the small dynamic variations that result from currents induced in surrounding coils. A model was developed and revealed an optimum output energy density that was independent of the geometry and the coil. An energy harvesting figure of merit was then defined to enable a final comparison of the materials, encompassing both material characteristics and realistic applications. Under these working

conditions and with all costs considered, some low-magnetostriction materials appeared able to compete with giant magnetostriction materials.

Keywords: Magnetostriction, magnetostrictive coefficient, energy conversion, Ericsson cycle, energy harvesting, predictive model

I – Introduction

The increasing numbers of wireless devices in use as a result of the rapid growth of the Internet of Things (IoT) [1] has led to the development of dedicated wireless sensors [2]. This development has highlighted the urgent need for alternative energy sources to replace batteries, which suffer drawbacks such as limited lifespans due to self-discharge and can cause severe pollution [3]. One widely studied solution is energy harvesting [4] based on smart materials. Various energy types can be collected [5] and converted into suitable electricity. Some energy harvesters for autonomous sensors are already commercially available [6].

A complete energy harvester includes three essential components: the active material [7][8], the structure, and the electrical interface [9][10]. Harvesters can be classified based on the type of energy source, e.g., as thermal energy harvesters (using thermoelectric materials [11]), solar energy harvesters (photovoltaic materials [12][13]), and vibrational energy harvesters (piezoelectric [14] or magnetostrictive materials [15–17]).

Among these energy sources, vibration is attractive because of its ubiquity (with sources ranging from human motion [18] to transportation modes such as aircraft [19] and railways [20]) and its availability even under relatively harsh conditions [21] (including enclosed spaces without access to light, and at moderately high temperatures).

Mechanical vibrations can be converted into electricity using magnetic or piezoelectric materials. The latter materials exhibit high output impedance and high output voltages [22][23], thus making them less flexible with regard to electrical energy treatment. Therefore, in this study, we focused preferentially on magnetostrictive materials.

The magnetostrictive effect was first observed in 1842 by Joule, who showed that application of a magnetic field could induce material deformation [24][25]. In 1865, Villari introduced the inverse effect by applying mechanical stress to cause changes in magnetization [26]. Magnetostrictive materials have numerous applications, including sensing [27], micropositioning, active vibration control [28], and biomedical applications [29]. The associated energy harvesters convert applied mechanical stress into a change in the magnetic flux density (the Villari effect [30]), which then produces an electromotive force across a wrapped coil that acts as an electrical generator.

The conversion process is associated with magnetic flux variations that can be performed using two methods: geometrically-induced reluctance change in the magnetic circuit [31][32] or the direct magnetostrictive effect [33]. The first method can be realized by geometrical transformation, including for example by varying the distance between the magnetostrictive material and a magnet (with an airgap). This solution can be implemented easily by adding an air gap to the magnetic circuit, although at the cost of a potential loss of integrability. However, the role of magnetostriction may be secondary when compared with the geometry change effect in this case. For systems using the magnetostrictive effect only, an optimized biasing magnetic field and optimized pre-stress level must be set according to the material's nature [34–36]. The objective is to achieve optimal operating conditions and use the magnetostrictive properties fully, i.e., realize the highest possible Villari effect.

Descriptions of vibrational harvesters that use both magnetostrictive and geometric reluctance variation effects can also be found in the literature [37], in which magnets provide the magnetic bias field to the material (e.g., Galfenol alloy [38]). During vibration periods, the distance variations between the sample and the magnet generate field changes and induce electromotive forces across the wrapping coils. However, when the two effects interact, the contribution of the highly magnetostrictive and expensive rare earth-based materials (10000–20000 €/kg for Terfenol-D and 5000-10000 €/kg for Galfenol [39]) becomes questionable.

To date, the literature on energy conversion materials for use in magnetostrictive energy harvesters has mostly focused on highly magnetostrictive materials [40–43]. Some references have been made to Metglas [44–46] and to FeCo in [47]. However, Terfenol-D has also shown brittleness under tensile stress [48], or a requirement for pre-stressing [49]. Therefore, materials with low magnetostriction should be investigated as potential conversion materials.

Most currently available review articles focus on evaluating the overall performance of the magnetostrictive energy harvesting system without exploring the potential energy conversion performance at a material level. Furthermore, the magnetic characterization data collected from the literature are gathered under differing conditions, including various magnetic field ranges and stress levels. A fair and comprehensive comparison of the magnetostrictive materials that is independent of the structures used has still to be provided. In this work, a broad comparison of magnetostrictive materials for energy harvesting applications is proposed that considers their potential energy density conversion performances under various magnetic field and mechanical stress operating conditions.

The first objective of the study is to verify whether cost-effective, low-magnetostriction materials can replace more expensive highly magnetostrictive materials under specific conditions and to assess these conditions. The materials assessed in this comparison are not limited to high-magnetostriction materials such as Galfenol and Terfenol-D. Instead, the study includes various ferromagnetic materials, e.g., electrical steels, nickel, iron-cobalt alloys, and amorphous strips (Metglas), which have costs that are more compatible with the battery replacement objective.

A common model was developed to estimate the anhysteretic magnetization curves for the materials under any specified stress within ±50 MPa through a fitting process. Theoretical thermodynamic Ericsson cycles were used to evaluate the output energy densities of the different materials. The area of the thermodynamic Ericsson cycles represents the energy density. Initially, without any limitations, cycles with a stress level of ±50 MPa were established with the aid of this model. The enclosed area was estimated under an unlimited magnetic field to represent the ultimate energy density of each material. In practical situations, the harvesting process is based on application of a bias magnetic field and the associated optimal working conditions must also be considered. The magnetoelastic coefficient was therefore estimated for each material as a function of the bias magnetic field. Finally, in realistic implementations, the dynamic magnetic field is produced by the currents induced in the surrounding coils, thus leading to a self-induced excitation situation, and the bias magnetic field is always imposed using a permanent magnet. A system model is proposed to derive the energy density that can be harvested and a figure of merit is proposed for comparison of the materials.

The structure of this manuscript is as follows. Section II describes the general state of the art, along with a comparison of multiple magnetostrictive energy harvesters presented in

the literature. Section III describes the numerical method used to simulate the magnetic anhysteretic curves. The model is validated through a fitting process and used to interpolate the data from the literature. Section IV presents the different estimation methods, including the thermodynamic Ericsson cycles under high field and stress conditions, and under low magnetic fields. For situations in which a bias magnetic field is used, the magnetoelastic coefficient's dependence on the magnetic field is discussed. Finally, the realistic case of the self-induced dynamic excitation field (i.e., through a magnet for magnetic bias and through a surrounding coil for induced current) is presented along with a comparison between the materials based on a figure of merit for energy harvesting. Using this approach, a brief comparison of the different methods is presented in Section V.

II – Energy harvester comparison

An initial comparison of energy harvesters from the literature from a device perspective is presented in table 1. The coupling effect is specified as either geometric reluctance variation or the Villari effect. Among the systems considered, the structures in [50] and [51] included a variable airgap between the magnet and the magnetostrictive material. During gap variation, the height of the airgap changes, which then causes a huge variation in the reluctance caused by the magnet. In this case, the main conversion mechanism is geometric reluctance variation. For all other energy harvesters listed in table 1, a constant distance was maintained between the magnet and the magnetostrictive materials, which means that the variation of the reluctance of the magnetic circuit comes from the magnetostrictive materials. In this case, the main effect used was the Villari effect. The conversion capabilities are given in terms of either energy density (J/cm^3) or power (mW), from which we derived W_{system}, W_{coil}, and $W_{material}$ to represent the energy densities with respect to the complete

device volume, the energy density with respect to the volumes of both the smart material and the coil, and the energy density with respect to the smart material volume alone, respectively. When the geometrical dimensions were not provided, estimates were made from the images of the devices.

Material	Main conversion mechanism	Frequency (Hz)	Output power (mW)	W_{system} (μJ/cm^3)	W_{coil} (μJ/cm^3)	$W_{material}$ (μJ/cm^3)	Ref.
Galfenol	Geometric reluctance variation	166	3.7	21	300	572	[50]
	Villari effect	140	0.63	1.5	4.1	48.6	[52]
	Villari effect	0.35	-	-	-	5	[53]
Terfenol-D	Geometric reluctance variation	-	-	187	1580	4400	[51]
	Villari effect	300	83	17.3	-	40.7	[54]
Metglas	Villari effect	300	-	-	-	1	[35]
	Villari effect	324	1.0	0.86	0.86	18.6	[55]
FeCo	Villari effect	64	0.0015	0.003	0.053	0.069	[56]
	Villari effect	50k	1.6	0.001	0.01	0.13	[57]

Table 1 – Comparison of energy harvester systems described in the literature. The parameters comprise the main conversion mechanism type; the working frequency (Hz); the output power; the device volume energy density; the coil and smart material volume energy density; and the smart material volume energy density.

Systems based on Terfenol-D and Galfenol showed higher W_{system} values than those based on Metglas and FeCo. However, the energy density of the complete system is highly dependent on the system's mechanical structure. Furthermore, some of these systems were designed as characterization setups rather than as energy harvesters. Therefore, the energy densities of the materials were compared, revealing that systems using the geometric reluctance variation mechanism are extremely advanced when compared with the other devices at a cost of lower integrability. However, Metglas can achieve an energy density of the same order as that of Terfenol-D and Galfenol, although it has much lower magnetostrictive activity (41 ppm [58] versus 1600 ppm for Terfenol-D [59] and >100 ppm for Galfenol [60][61]). Therefore, some materials with low magnetostriction that have barely

been investigated to date should be considered to achieve similar performances under low magnetic fields.

In fact, the geometric reluctance variation is always used in the variable reluctance energy harvester, which is a specific harvester type that differs from magnetostrictive energy harvesters. The variable reluctance energy harvester is always composed of a rotating toothed wheel and a stationary pickup setup [62]. The pickup setup is similar to that of the magnetostrictive energy harvester, composed of a conversion material, a magnet, and coils. Because the conversion depends on Faraday's law, the conversion material must be magnetic, but is not necessarily magnetostrictive.

However, among the energy harvesters that use magnetostrictive materials, some devices mix the variable reluctance effect with the magnetostrictive effect. Figure 1 highlights the structural influence. With the same material, systems that use the geometric reluctance variation method could show energy density levels up to two orders of magnitude higher the devices that use the Villari effect alone. These conclusions raised questions about the intrinsic conversion abilities of each material independently of their structure. It is thus necessary to make a fair comparison at the material level.

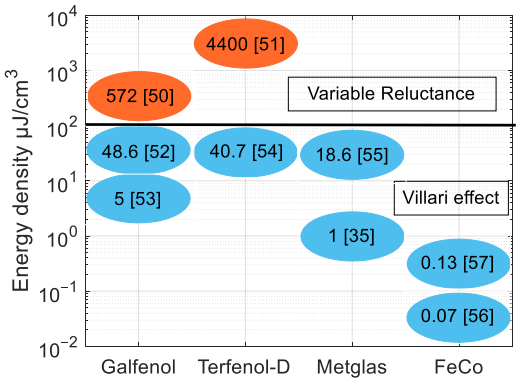

Figure 1 – Comparison of energy harvester systems that use the geometric reluctance variation method and the Villari effect.

III – Numerical method for simulation of anhysteretic behavior

This section focuses on the development of a numerical method to simulate the anhysteretic behavior. The anhysteretic curves are reconstructed using data collected from the literature. The objective of this approach is to reproduce the anhysteretic curves numerically. These simulations constitute a first step toward estimation of the energy conversion abilities of the magnetostrictive materials.

3.1 Estimation of the anhysteretic curves

Although some materials may appear unsuitable for energy harvesting at first glance, their cost and availability make them worthy of investigation. In addition to the classical Galfenol and Terfenol-D, the magnetostrictive materials listed below were also tested:

- FeCo alloy [63][64]. This material was investigated for use in energy harvesting. Additionally, the various alloy compositions have a wide range of applications, including actuators, transducers, and motors. The composition 48Fe-50Co-2V (referred to as FeCo-2V hereafter) was selected because of the availability of its magnetic hysteresis curves under different stress levels.
- Two grades of grain-oriented electrical steel [65][66]: highly grain-oriented (referred to as HGO hereafter) and conventional-grade grain-oriented (referred to as CGO hereafter) electrical steel. These alloys are used intensively as laminated magnetic core materials for power conversion. Their magnetic performances (e.g., magnetostriction) are well documented.
- A non-oriented grain electrical steel (referred to as FeSi NO hereafter [67][68]). This material is mainly used in electric motors.
- A pure nickel alloy [69]. This material is characterized by the highest reported magnetostriction among the pure elements.

- As cast CoFeSiB (referred to as AC CoFeSiB hereafter) and Annealed CoFesiB (denoted as A CoFeSiB hereafter) amorphous ribbon [70–72]. These materials are normally used in sensing applications.
- As grown Galfenol (denoted as AG Galfenol hereafter) and Annealed Galfenol (referred to as A Galfenol hereafter) [73]. Galfenol can be processed in a way that incorporates an internal, customized pre-stress into the material. This pre-stress, known as stress-annealing, enables the material to exhibit a magnetostrictive response even when subjected to tensile loads exceeding 50 MPa.

This work investigated the conversion capabilities of these materials based on their magnetic properties under static stress. Abundant information on these materials can be found in the literature, thus allowing extraction of the required data for the comparison process, with results as presented in figure 2.

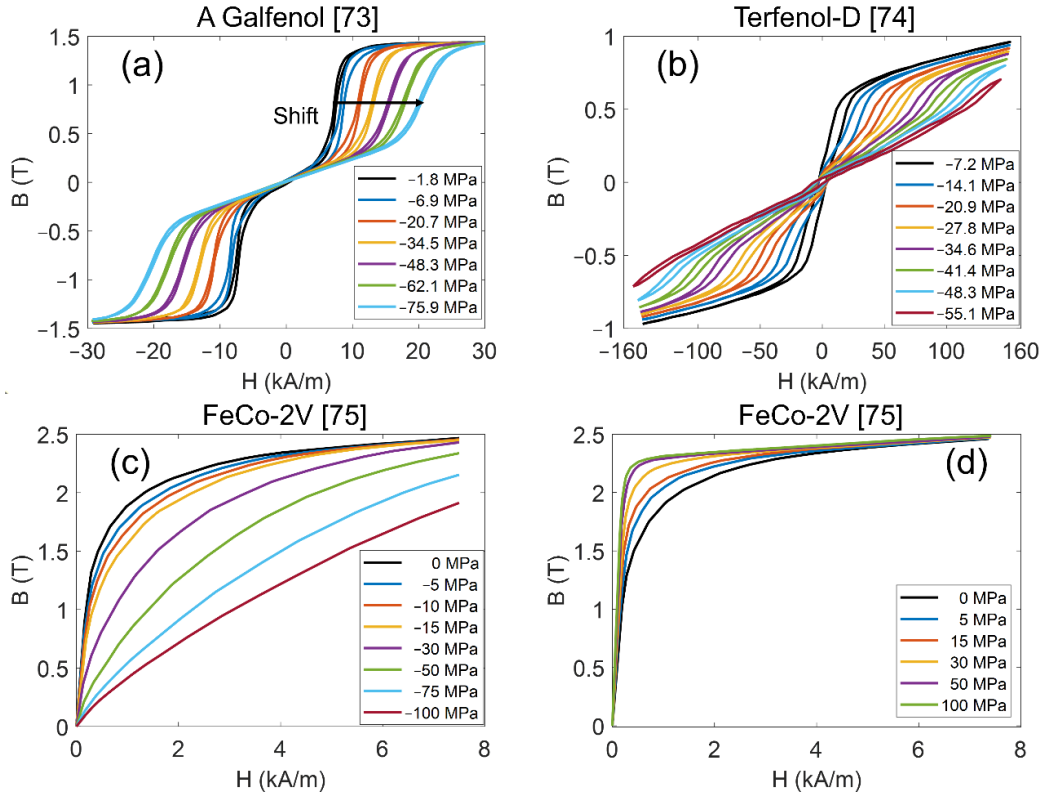

Figure 2 – Magnetic characterization of (a) A Galfenol under compressive stress [73], (b) Terfenol-D under compressive stress [74], (c) FeCo-2V under compressive stress [75], and (d) FeCo-2V under tensile stress [75].

The characterization results for Galfenol and Terfenol-D are shown as magnetic hysteresis curves in figure 2(a) and (b), respectively, while the FeCo-2V characteristics under tensile and compressive stress are given in the anhysteretic curves shown in figure 2(c) and (d), respectively. Anhysteretic curves were estimated for materials with hysteresis curves by averaging their major hysteresis cycle's ascending and descending branches, as illustrated in figure 3. We assumed that no variations occurred in the external conditions during each complete magnetization cycle.

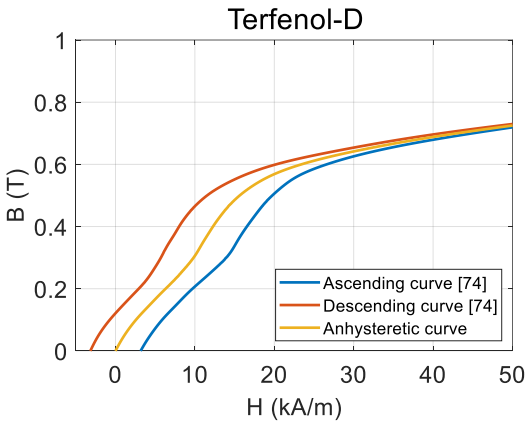

Figure 3 – Illustration of anhysteretic curve estimation from a hysteresis cycle [74].

3.2 Range of investigations

Collection of the data from various studies resulted in different stress levels being applied from one material to another. Therefore, homogenous test conditions are essential to compare the energy conversion capabilities correctly. In this work, a simulation method was developed to predict/interpolate the material magnetic responses under common stress and magnetic field levels.

With regard to mechanical stress levels, apart from CGO and Metglas 2605SA1, which were limited to –10 MPa and ±30 MPa, respectively, all other materials had available characterizations up to ±50 MPa (table 2). Additionally, it is possible to apply this stress level under realistic conditions based on the stress levels reached in devices (0.106 N for a FeCo

specimen in [56] ≈ 7.5 MPa, plus 30 MPa [51] and 50 MPa [76] for Terfenol-D and Galfenol, respectively). Eventually, we opted for ±50 MPa as uniform stress conditions.

Materials	Mechanical range of collected *BH* curves	Mechanical excitation in devices
FeCo-2V	−100 to 100 MPa [75]	0.106 N [56]
Terfenol-D	−55.1 to −7.2 MPa [74]	20 to 30 MPa [51]
A Galfenol	−75.9 to 51 MPa [74]	50 MPa [76]
FeSi	0 to 67 MPa [77]	-
Nickel	0 to 120 MPa [78]	-
CoFeSiB	0 to 180 MPa [79]	-
FeSi NO	−100 to 100 MPa [75]	-
HGO	0 to 118 MPa [80]	-
CGO	−10 to 0 MPa [81]	-
Metglas 2605SA1	−30 to 30 MPa [82]	4 MPa [35]

Table 2 – Mechanical stress ranges for the data collected from the literature.

B: magnetic flux density; H: magnetic field strength.

3.3 Anhysteretic biphasic model definition

Figure 2(a) depicts the typical Galfenol B(H) hysteresis cycles measured under various compressive stress levels [73]. Low permeability and reversible behavior are both observed in the Rayleigh region [83][84]. The limit of this region increases with increasing stress and induces two additional inflexion points in the typical ferromagnetic sigmoid anhysteretic behavior. In figure 2(b), the Terfenol-D [74] curves are not saturated within the magnetic field range considered and show non-negligible linear increasing components under high fields.

The curves of FeCo-2V under compressive stress are shown in figure 2(c) as the typical shape characteristics for the other materials. Compressive stress reduces this material's magnetic flux density and permeability, similar to Terfenol-D. Figure 2(d) shows the tensile stress curves for the same material, showing similar mechanisms but yielding magnetic property shifts in the opposite direction. Rapid saturation is observed under all stress levels.

In [85] and [86], a nonlinear function was proposed to describe the magnetic behavior of Terfenol-D. A biphasic model was developed in [82] for Metglas 2605SA1, which focuses more on mathematical description rather than phenomenological approach. In this approach, a hyperbolic tangent function and a linear term are chosen as it provides a sigmoid shape that fits well with the magnetic hysteretic curves of considered magnetostrictive materials. As the focus of this work lies in the material aspect, the stress dependence of the shifting behavior (associated with an activation mechanism of the magnetostrictive coupling) observed at the Rayleigh region of Galfenol (figure 2(a)) is included as well. In that case, a term $\pm(H_0+\eta\sigma)$ is added, where H_0 denotes the magnetic excitation shift related to a potential transition in the material that originates from the observed activation mechanism in some compositions, and η is the correlation between this shift and the stress level. The improved equation is presented as follow:

$$B = \alpha\frac{1}{\pi}\arctan[\beta(1+\tanh(\gamma.\sigma))(H-(H_0+\eta.\sigma))]+\alpha\frac{1}{\pi}\arctan[\beta(1+\tanh(\gamma.\sigma))(H+(H_0+\eta.\sigma))]+(\mu-\kappa.\sigma)H \quad (1)$$

where α represents the magnetic flux density saturation of the nonlinear part, β is the small-signal slope of the nonlinear part, yielding $2\alpha\beta/\pi$ as the linear permeability of the nonlinear part (i.e., a linearization of the nonlinear function for small excitation levels). Additionally, μ is the zero-stress permeability of the linear part, and γ and κ are the magnetoelastic coefficients of the nonlinear and linear phases, respectively.

3.4 Simulation results and validation

The simulation parameters for each material were determined using the Matlab® Curve Fitting Toolbox. To this end, the reasonable range of the parameters was first estimated, along with a consistent and realistic working point. Under these conditions, using the Nonlinear Least Squares Method and the True-Region algorithm, the toolbox would provide

the optimal set of parameters to align the equation with the anhysteretic curves derived from the experimental data at various stress levels. Typical simulation results and comparisons of these results with anhysteretic curves obtained from the experimental data are shown in figure 4. Two applied stress levels were tested for each material. The results showed good agreement between the model and the corresponding anhysteretic curves at all magnetic field levels, thus validating the proposed simulation method.

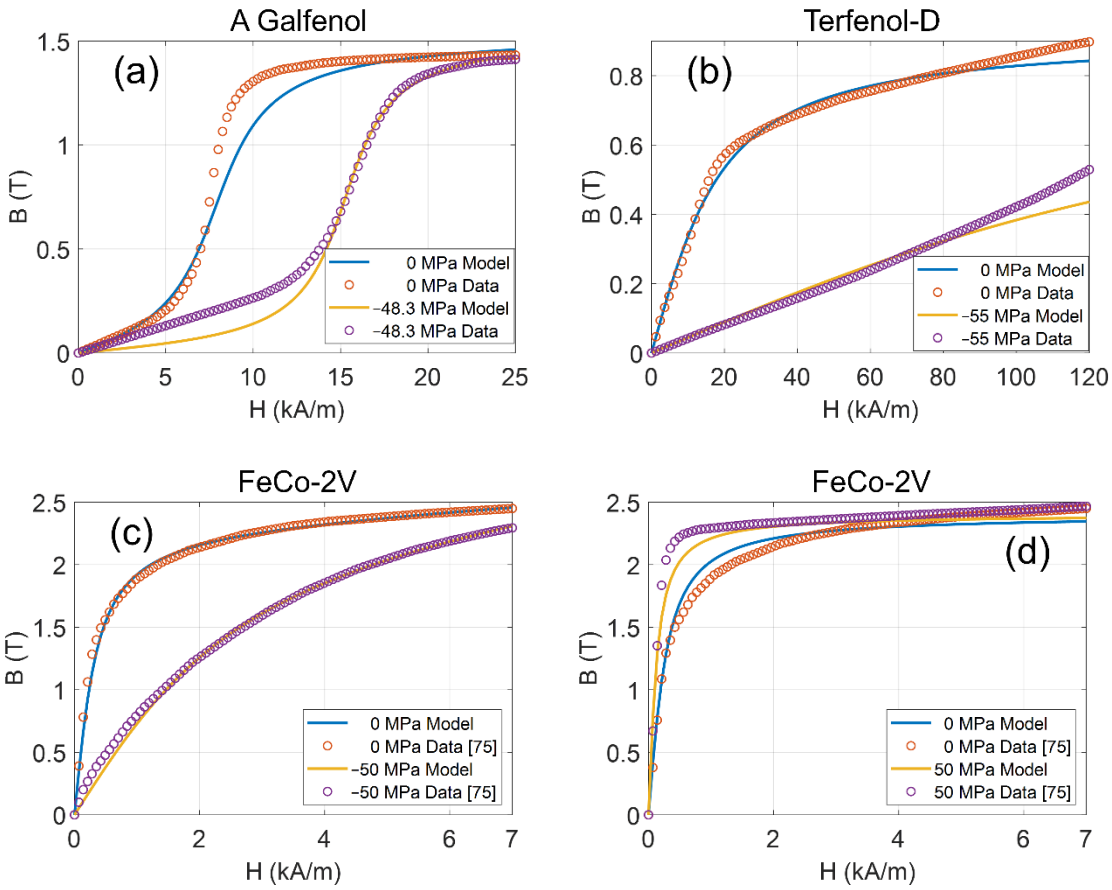

Figure 4 – Curve fitting results for (a) A Galfenol under compressive stress, (b) Terfenol-D under compressive stress, (c) FeCo-2V under compressive stress, and (d) FeCo-2V under tensile stress.

Parameters and validation have also been completed for the other materials. All the simulation parameters and the references to the experimental data are listed in table 3 for

the tensile stress case and table 4 for the compressive stress case. Each material's coefficient of determination R^2 (Eq. (2)) was then calculated to check the simulation method's accuracy:

$$R^2 = 1 - \frac{\sum_i (y_i - f_i)^2}{\sum_i (y_i - \bar{y})^2} \quad (2)$$

Here, y_i and $\bar{y}$ represent the experimental magnetic flux density for each material and its mean value, respectively. f_i represents the corresponding value predicted using the simulation method. An R^2 value that is closer to 1 indicates a better fit to the data [87]. All coefficients of determination are listed in tables 3 and 4. Their values are all >0.9, confirming the simulation method's high accuracy.

Materials	λ (ppm)	α (T)	β (m·A^{-1})	γ (Pa^{-1})	H_0 (A·m^{-1})	η (A·m^{-1}·Pa^{-1})	μ (T·m·A^{-1})	κ (T·m·A^{-1}·Pa^{-1})	R^2	Ref.
FeSi NO	3.6	1.3	0.0026	9.5×10^{-7}	-	-	10^{-5}	-3.6×10^{-14}	0.97	[75]
Metglas 2605SA1	41	1.4	0.006	7×10^{-7}	-	-	8×10^{-5}	2.5×10^{-14}	0.97	[82]
A Galfenol	250	1.8	2.9×10^{-4}	5.9×10^{-9}	1×10^{4}	-1.7×10^{-4}	-	-	0.99	[73]
HGO	−0.35	1.7	0.041	-8.6×10^{-9}	27.4	5.7×10^{-7}	-	-	0.99	[80]
FeSi-90°	3	1.3	0.033	1.8×10^{-8}	125	-2.1×10^{-6}	-	-	0.99	[77]
FeSi-55°	−17	1.1	0.05	-9.4×10^{-9}	47	1.4×10^{-6}	-	-	0.99	[77]
FeSi-0°	−27	1.7	0.12	-1×10^{-8}	-	-	-	-	0.98	[77]
Nickel	−40	0.5	4.6×10^{-4}	-1.6×10^{-8}	-	-	-	-	0.99	[78]
AC CoFeSiB	−0.11	0.7	0.01	-4.5×10^{-9}	-	-	-	-	0.96	[79]
A CoFeSiB	0.095	0.6	0.015	3×10^{-7}	-	-	-	-	0.96	[79]
FeCo-2V	25	2.4	0.004	5×10^{-7}	-	-	-	-	0.94	[75]

Table 3 –Simulation parameters and their corresponding coefficients of determination for the tensile stress case.

Materials	λ (ppm)	α (T)	β (m·A^{-1})	γ (Pa^{-1})	H_0 (A·m^{-1})	η (A·m^{-1}·Pa^{-1})	μ (T·m·A^{-1})	κ (T·m·A^{-1}·Pa^{-1})	R^2	Ref.
AG Galfenol	160	1.4	7.7×10^{-4}	-1.4×10^{-9}	936	-1.9×10^{-4}	-	-	0.99	[73]
A Galfenol	240	1.6	4.5×10^{-4}	-2.2×10^{-9}	7876	-1.5×10^{-4}	-	-	0.98	[73]
CGO	1	1.8	0.126	9.2×10^{-8}	-	1.4×10^{-5}	-	-	0.99	[81]
FeSi NO	3.6	1.4	2×10^{-3}	1.6×10^{-8}	-	-	1.2×10^{-6}	-5.73×10^{-13}	0.99	[75]
FeCo-2V	25	2.3	3.4×10^{-3}	2.6×10^{-8}	-	-	3×10^{-5}	-5.97×10^{-13}	0.99	[75]
Metglas 2605SA1	41	1.4	5.5×10^{-3}	3.6×10^{-8}	-	-	8×10^{-5}	2.652×10^{-14}	0.99	[82]
Terfenol-D	1400	0.9	6.5×10^{-5}	2.5×10^{-8}	-	-	-	-	0.94	[74]

Table 4 –Simulation parameters and their corresponding coefficients of determination for the compressive stress case.

IV – Evaluation of energy harvesting density

This section presents estimates of the energy that is harvestable under different limitations. Anhysteretic curves at σ = 0 MPa and ±50 MPa were simulated using the numerical method. The theoretical converted energy was then calculated based on specific assumptions. To avoid significant discrepancies for CGO and Metglas 2605SA1, their stresses were limited to –10 MPa and ±30 MPa, respectively, corresponding to the ultimate stress levels tested for these materials in the literature.

4.1 Ultimate energy density of the Ericsson cycle

The thermodynamic Ericsson cycle is helpful when estimating the ultimate converted energy density [88][89]. An Ericsson cycle consists of two steps that are performed under constant stress and two other steps that are performed under a constant field [90][91]. As figure 5(a) shows, it is possible to reconstruct an Ericsson cycle from a pair of anhysteretic curves acquired at different stress levels. The constant stress steps follow the anhysteretic trajectories. The constant field steps represent vertical jumps from one anhysteretic curve to the other. The area enclosed by the resulting Ericsson cycle then represents the converted energy density. Beyond a threshold level in the high field range, the stress and no-stress anhysteretic curves merge, as depicted in figure 5(b). Application of larger fields will not modify the energy density beyond this level and the resulting Ericsson cycle area can be regarded as the material's ultimate energy density.

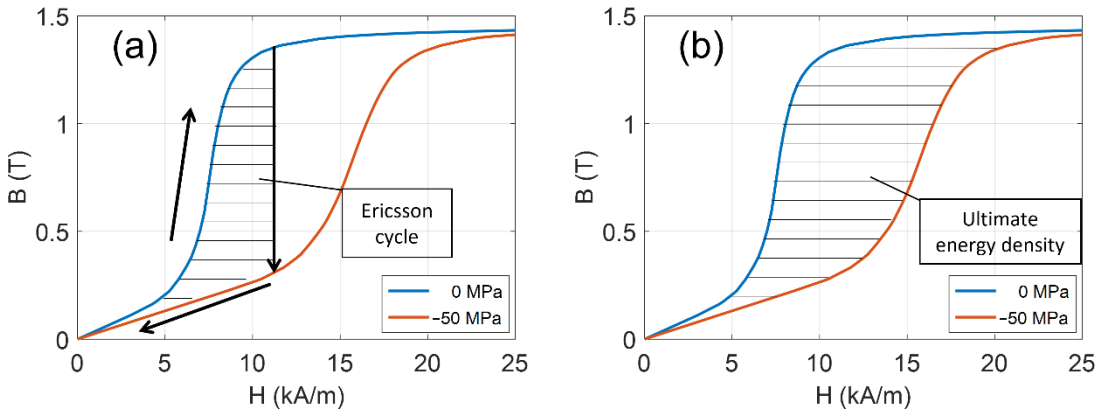

Figure 5 – (a) Ericsson cycle example and the associated converted energy density. (b) Ultimate energy density under a high magnetic field.

The tested materials showed significant differences among their magnetic field responses. Additionally, the compressive and tensile stresses induced opposite effects. In the Terfenol-D case, the curves were not merging at 150 kA/m, which is the maximum magnetic field applied in the literature. With the exception of Terfenol-D, the magnetic field range studied in this work (15 kA/m under tensile stress and 150 kA/m under compression) is high enough to observe merging of the flux densities for the stress-free and stressed cases. Therefore, to reach reasonable levels and realize reliable comparisons, the ultimate energy density was estimated to be H = 15 kA/m for the tensile stress case and H = 150 kA/m for the compressive case.

All simulated anhysteretic curves under compressive and tensile stress conditions and under low and high magnetic fields are compared in figure 6. Because the anhysteretic curves for most materials were approximately merged under low magnetic fields, all materials are first presented and compared as shown in figure 6(a) and (c) under low magnetic fields. Materials that do not exhibit merged flux densities under low magnetic excitation are presented in figure 6(b) and (d). Additionally, because this work is intended to establish the ultimate energy density at the material level, only the curves with the highest

energy densities for each material are shown to provide a clearer comparison. In the case of grain-oriented silicon steel characterized by highly anisotropic magnetic properties [92][93], the energy density is dependent on the magnetic field direction (where 0° is the rolling direction RD and 90° is the transverse direction TD), as expected, and the highest energy point (90°) was thus retained.

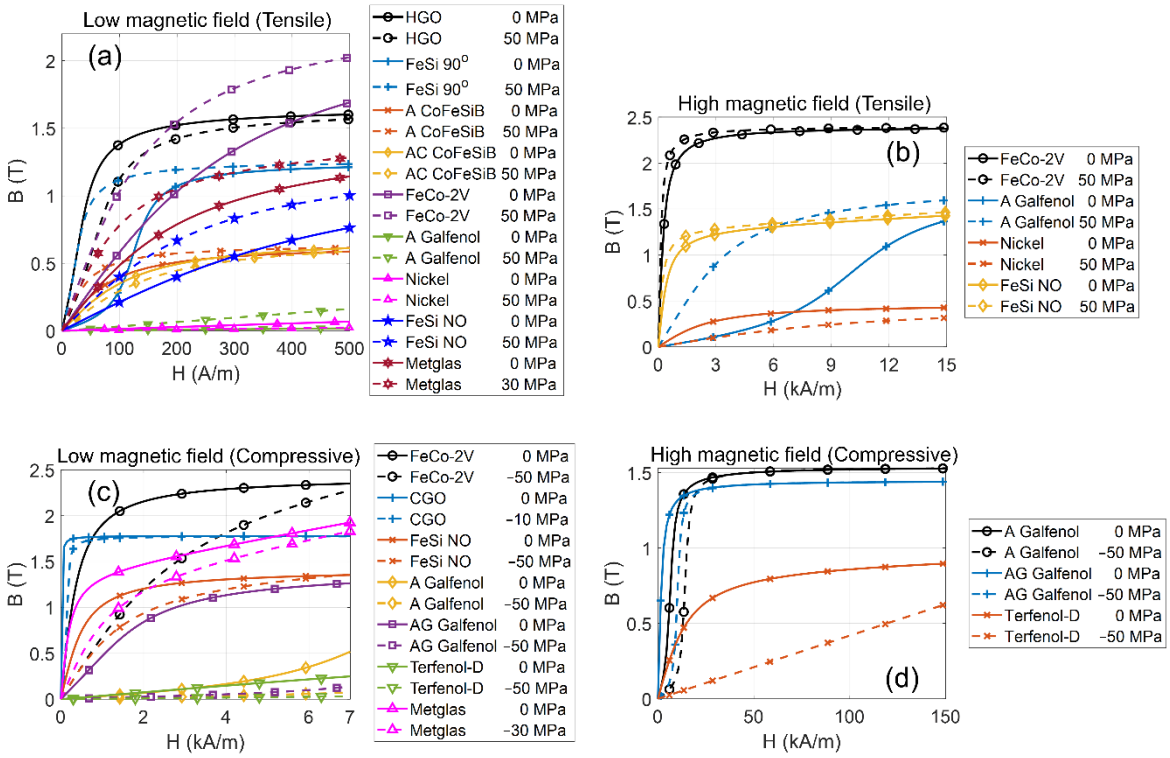

Figure 6 – Simulated Ericsson cycles for all materials tested under both compressive and tensile stresses and within low and high magnetic field range.

Then, all energy densities in the 0–15 kA/m range for σ = 50 MPa and those in the 0–150 kA/m range for σ = −50 MPa were calculated and plotted versus the magnetostriction strain λ, with results as depicted in figure 7. For the materials for which the magnetization curves under ±50 MPa conditions were available from the literature, the energy density was derived from the experimental data directly. Within this magnetic field range, most Ericsson cycles were formed by merging the anhysteretic curves under high field conditions, meaning

that the ultimate energy density was obtained. The results show that materials with higher magnetostriction characteristics show higher energy densities.

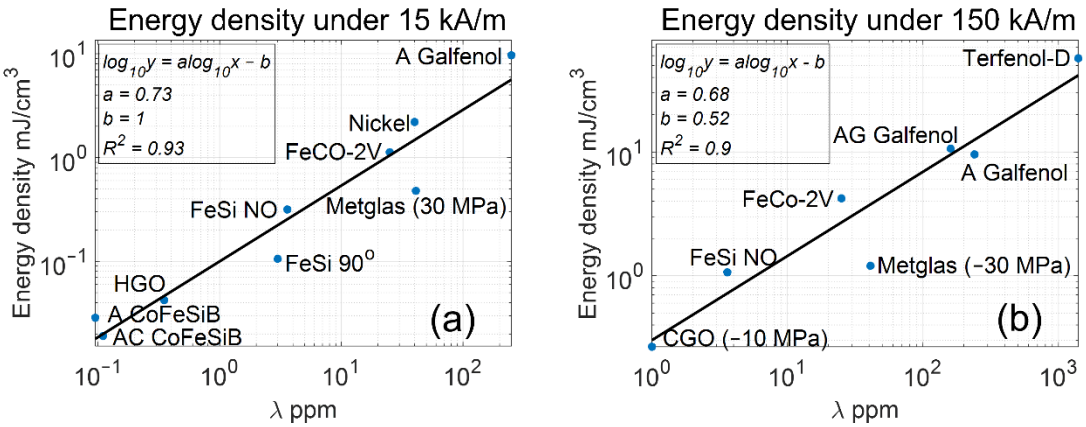

Figure 7 – Energy density vs. maximum magnetostrictive strain λ under conditions of (a) 0–15 kA/m and σ = 50 MPa, and (b) 0–150 kA/m and σ = −50 MPa.

We then established the link between the material model parameters, the maximum magnetostrictive strain λ, and the energy density of the materials. For this purpose, correlations were proposed through linear fittings of the logarithmic quantities (see Eq. (3)), where x represents the simulation parameters and y is the energy density.

$$\log_{10} \mathrm{y} = a \log_{10} \mathrm{x} - b \tag{3}$$

The fitting coefficients *a* and *b* were determined using the Matlab® Curve Fitting Toolbox, employing the Nonlinear Least Squares Method and the True-Region algorithm. The coefficient of determination R^2 were estimated for each correlation attempt at two magnetic field levels (with 1 kA/m representing the low field range, and 15–150 kA/m for the high field range). The results are summarized in table 5. The R^2 for λ exceeded 0.9 for both the tensile and compressive cases, verifying the excellent quantitative correlation between the ultimate energy density and λ. The other parameters did not show any particular correlation. Negative values of R^2 were observed in the absence of correlation (when the average of the squared residuals became greater than the variance).

Parameter	Tensile stress 0–15 kA/m			Compressive stress 0–150 kA/m		
	a	b	R^2	a	b	R^2
λ	0.73	1	0.93	0.68	0.52	0.9
α	1.33	0.73	−0.1	−3.41	−1.15	0.07
β	−1.06	3.03	0.72	−0.71	1.35	0.86
2αβ/π	−0.81	2.52	0.43	−0.65	1.2	0.83
γ	0.07	0.07	−0.17	−0.69	5	0.37

Table 5 – Fitting coefficients for each simulation parameter with their corresponding coefficients of determination under high magnetic field conditions.

High linear permeability leads to saturation within the low field range, regardless of the mechanical stress status. Therefore, the Ericsson cycle tended to enclose a smaller area within that range, which resulted in a lower energy density. Nonetheless, this conclusion is related to the material's behavior only, it does not provide information about the magnetoelectric energy conversion associated with the structure itself including coils. This point is addressed in detail in section 4.3. In that case, 2αβ/π, which represents the small-field permeability of the nonsaturated nonlinear phase under zero stress, influenced the energy density strongly. However, for the materials that showed stress-dependent shifting of their Rayleigh region boundaries (Galfenol and FeSi), the 2αβ/π parameter cannot be used to predict the magnetic behavior under stress precisely.

Theoretically, through consideration of the reciprocity of the Villari effect and the magnetoelastic coefficient, good correlation was expected between the Ericsson cycle energy density and λ. Both parameters can be expressed using Maxwell's relationship:

$$\theta = \frac{\partial \mathrm{B}}{\partial \sigma} = \frac{\partial \lambda}{\partial \mathrm{H}} \tag{4}$$

In fact, λ and the converted energy are both integrated values of the same magnetoelastic coefficient. The total magnetostrictive strain λ_{max} is given by:

$$\lambda_{\max} = \int_0^{\mathrm{H}_{\max}} \frac{\partial \lambda}{\partial \mathrm{H}} \mathrm{dH} = \int_0^{\mathrm{H}_{\max}} \frac{\partial \mathrm{B}}{\partial \sigma} \mathrm{dH} \tag{5}$$

and thus the ultimate Ericsson cycle energy density W_{max} can be obtained as the integral of this expression over the stress range considered:

$$W_{max} = \int_{\sigma_{min}}^{\sigma_{max}} \int_{0}^{H_{max}} \frac{\partial B}{\partial \sigma} dH d\sigma \quad (6)$$

If the Villari coefficient is independent of σ, then the energy density becomes proportional to λ:

$$W_{max} = (\sigma_{max} - \sigma_{min}) \int_{0}^{H_{max}} \frac{\partial B}{\partial \sigma} dH d\sigma = (\sigma_{max} - \sigma_{min}) \lambda_{max} \quad (7)$$

Ultimately, the excellent correlation between λ and the Ericsson cycle energy density obtained within the high field range suggested that the magneto-mechanical coupling had a weak dependence on the mechanical stress σ.

The ultimate energy density of each material shows its individual potential as a conversion medium for an energy harvester in the ideal case, in which the magnetic field is controlled continuously using an ideal amplifier and coil system.

However, when the magnetic field is limited, the curves that form the Ericsson cycle do not merge, as shown in figure 5(a). In that case, the area that is enclosed by the anhysteretic curves is obviously dependent on the shapes of the curves. The energy densities at ±50 MPa and 1 kA/m were calculated and plotted vs. the magnetostrictive strain λ (figure 8).

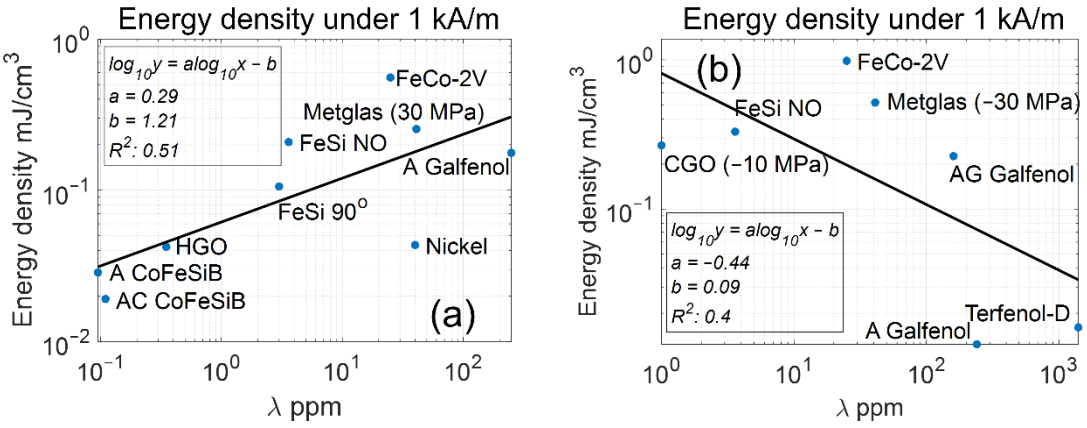

Figure 8 – Energy density characteristics for (a) tensile stress and (b) compressive stress under low magnetic field (1 kA/m) conditions.

Here, the low-magnetostriction materials show energy densities of the same order of magnitude or even larger than those of the highly magnetostrictive materials. The correlation between magnetostriction and the Ericsson cycle energy density is illustrated in figure 8. R^2 was found to be always less than 0.6, indicating that the energy density was not correlated with λ.

The Ericsson cycle is helpful in describing the ideal harvesting process and in estimating the maximum energy for specified magnetic field and stress levels. A system performing an ultimate Ericsson cycle could potentially be envisaged for higher power cases similar to electrical machines (kW range and beyond), but is not reasonable within the energy harvesting framework (far below 1 W). Therefore, it cannot provide information about the feasibility of electrical/magnetic interfaces and can only be used to perform basic comparisons between the materials.

4.2 Investigation of the magnetoelastic coefficient

In the case of active control of the current in a surrounding coil, it may be considered possible to enhance the harvested energy independently of the magnetic permeability. In this case, the energy density would be directly proportional to the magnetoelastic coefficient $\theta = \frac{\partial B}{\partial \sigma}$, which is a function of both the mechanical stress and the magnetic field. For comparison purposes, we propose to calculate the average magnetoelastic coefficient [94] between 0 MPa and 50 MPa and to investigate its dependence on the magnetic field in this section. The results for Galfenol and Terfenol-D are given in figure 9. To provide a more accurate estimate, a sum of the local magnetoelastic coefficients under different bias

magnetic fields of σ_b = 10, 20, 30, 40, and 50 MPa was calculated to estimate the average magnetoelastic coefficient over the mechanical stress levels:

$$\frac{\Delta B}{\Delta \sigma} = \frac{1}{\Delta \sigma} \int_{\sigma_b - \frac{1}{2}\Delta\sigma}^{\sigma_b + \frac{1}{2}\Delta\sigma} \frac{\partial B}{\partial \sigma}\, d\sigma$$

$$= \frac{d\sigma}{\Delta \sigma} \times \Sigma \frac{\partial \mathrm{B}}{\partial \sigma} \quad (8)$$

These predictions, which were realized with the aid of the model, were confirmed by the experimental results shown in figure 9.

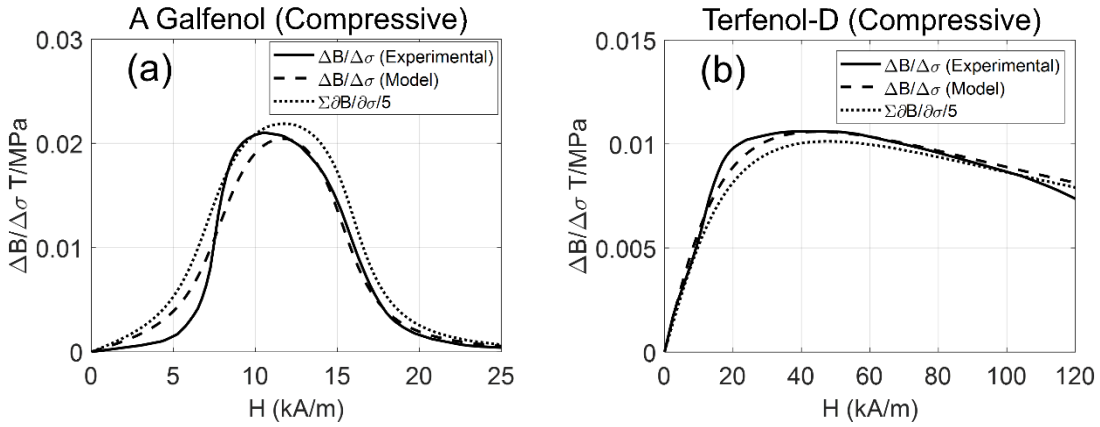

Figure 9 –Magnetoelastic coefficients derived from experimental and simulated anhysteretic curves for (a) Galfenol and (b) Terfenol-D.

For materials like Galfenol, an optimal local magnetoelastic coefficient that is much higher than the average value can be obtained under a given bias field, as shown in figure 9(a). Ideally, an energy harvester with A Galfenol should operate close to this optimal bias field (approximately 10 kA/m for σ = −50 MPa, as illustrated in figure 9(a)). Additionally, the structure should be optimized for an adapted ΔH that makes full use of the magnetoelastic coefficient application range to harvest as much energy as possible.

In contrast to Galfenol, Terfenol-D (figure 9(b)) shows only a weak dependence on the bias field amplitude, particularly after a threshold value of 2×10^4 A/m.

The magnetoelastic coefficients under ±50 MPa conditions were finally compared for all materials in Figures 10 and 11. The magnetoelastic coefficient's signs are consistent with the occurrence of magnetostriction.

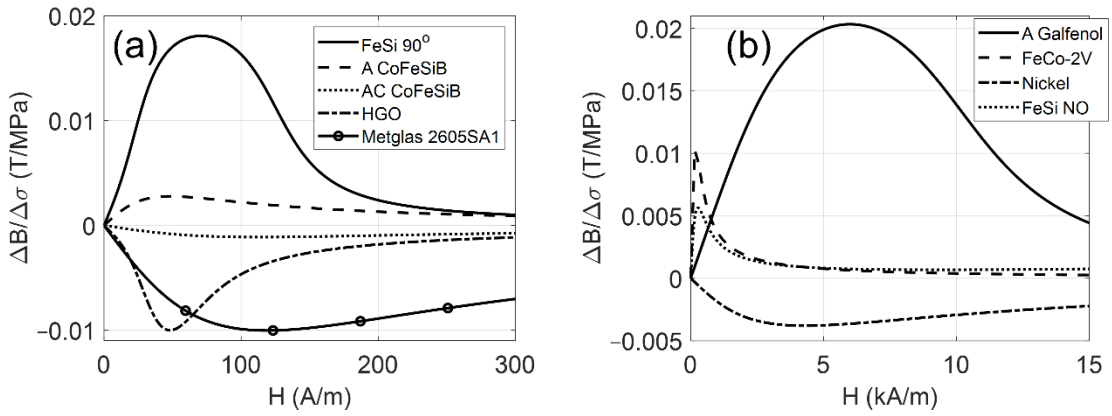

Figure 10 – Comparisons of magnetoelastic coefficients as obtained from the σ = 50 MPa simulated curves under (a) low magnetic fields and (b) high magnetic fields.

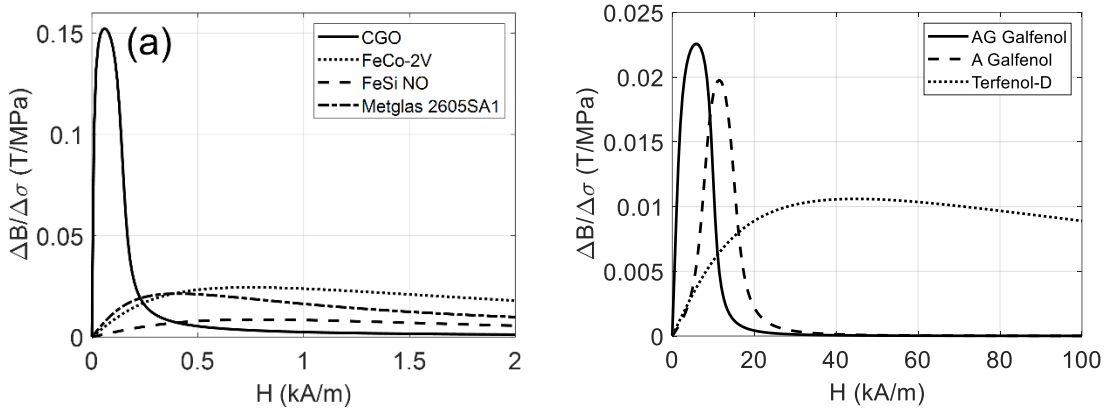

Figure 11 – Comparisons of magnetoelastic coefficients as obtained from the σ = −50 MPa simulated curves under (a) low magnetic fields and (b) high magnetic fields.

Under stress of 50 MPa (figure 10), most materials achieved optimal conversion under bias fields of less than 2 kA/m. Only nickel and Galfenol had higher optimal bias fields at 4 kA/m and 6 kA/m, respectively.

In figure 11(a), the magnetoelastic coefficient of CGO is one decade higher than the values for the other materials under compressive stress. However, because of the small magnetic field range, the energy density of CGO is limited to a low level, according to Eq. (6).

At σ = −50 MPa, CGO, FeCo-2V, and FeSi NO demonstrated reasonable optimal bias fields of less than 1 kA/m (figure 11(a)). In figure 11(b), Galfenol and Terfenol-D showed optimal fields close to 10 kA/m. Realization of such high-bias fields sounds challenging. In practical energy harvesters, permanent magnets are used to provide the bias fields. A high bias

magnetic field would mean use of oversized permanent magnets, leading to oversized harvesters. Furthermore, permanent magnets are characterized by their low permeability. A large permanent magnet would also eventually include high series reluctance in the case of a harvester with a closed magnetic circuit, thus reducing the overall magnetostriction coupling effect.

Note that for the energy harvesters described in [53], peak powers were obtained at 10 kA/m for AG Galfenol and at 15 kA/m for A Galfenol under compressive stress. In [59], the maximum magnetoelastic coefficient value of Galfenol was reached at 19.53 mT/MPa. This value shows very good agreement with the model estimate (figure 11). In the Terfenol-D case, magnetic bias of 63.66 kA/m (800 Oe) was required in [95] to achieve the highest coupling level. For this material, the model predicts slight variations in the magnetoelastic coefficient (figure 11(b)); therefore, the optimal 60 kA/m could be reduced to 20 kA/m without having any significant impact.

This investigation of the magnetoelastic coefficient provides a good indication for selection of the bias magnetic field required for a given material. However, some materials show a high magnetoelastic effect but a low energy harvesting capability, e.g., CGO. In that case, the coefficient value cannot provide a fair comparison between the materials because the effect of the stress levels has not been considered.

4.3 Second limitation – Bias magnetic field and self-induced dynamic magnetic field

In this section, the small cycle representing the practical energy harvesting process is presented. As a first investigation of the effect of the circuit, a linear load is taken into account, the harvested energy density and the magnetic optimum frequency were derived in the case of impedance matching. The linear load may mimic, as a first approximation, the

(potentially linearized) behavior of the electrical interface aiming at actually harvesting the energy (along with signal conditioning).

In practice, the typical structure comprises a rod- or bar-shaped magnetostrictive material, to which permanent magnets apply a bias magnetic field, and a surrounding coil connected to a load (mostly resistive loads with impedance matching). In this case, the magnetic field variations are caused by reluctance variations and induced currents in the coils, which act as a secondary magnetic field source in addition to the permanent magnet. Furthermore, the variation in the stress level depends on the vibration sources and is usually of low dynamic value. Therefore, the magnetic performance undergoes a relatively small cycle, with structure-dependent magnetic field and stress variations that cannot be predicted or controlled precisely. To harvest the maximum energy density, the cycle must be positioned within an optimum bias magnetic field and under optimal mechanical pre-stress. In that case, to harvest additional energy, the bias magnetic field and the pre-stress effect on the energy density were investigated to have the optimum working conditions.

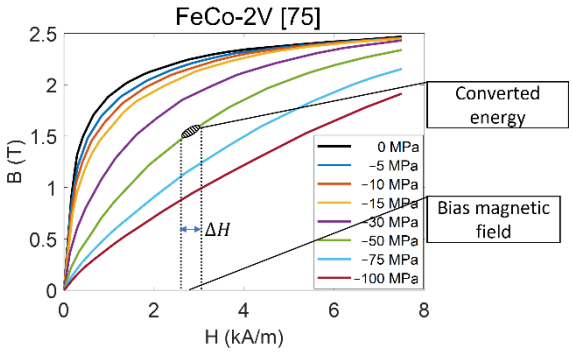

Figure 12 – Illustration of the energy harvesting process and the converted energy density attained in practical situations [75].

These working conditions lead to elliptical cycles [36][54][96–98], consisting of a bias field, a pre-stress associated with a dynamic magnetic excitation ΔH, and a dynamic mechanical excitation Δσ, as depicted in figure 12.

The area of the small loop that represents the converted energy realized from the material during the actual process can be described using:

$$W = -\pi \frac{\theta^2 \sigma_0^2}{\mu} \times \frac{\frac{\omega}{\omega_0}}{1+\left(\frac{\omega}{\omega_0}\right)^2} \quad (9)$$

where the details of the required calculation are presented in the Appendix. When the device operates at its optimal frequency, the maximum converted energy yields:

$$W_{max} = -\pi \frac{\theta^2 \sigma^2}{2\mu} \quad (10)$$

where the local magnetoelastic coefficient θ is $\frac{\partial B}{\partial \sigma}$, and σ and μ represent the amplitudes of the dynamic mechanical stress and the permeability, respectively. Assuming that the harvester is connected to a load with resistance matching (i.e., R_{load} = R_{coil}), the harvested energy on the load is half of the total energy converted from the material. This harvested energy, denoted by W_{load}, is given by the following equation:

$$W = -\frac{\pi}{2} \frac{\theta^2 \sigma_0^2}{\mu} \times \frac{\frac{\omega}{\omega_0}}{1+\left(\frac{\omega}{\omega_0}\right)^2} \quad (11)$$

In [35], Zucca et al. used an $Fe_{78}B_{13}Si_9$ ribbon under a peak dynamic load of 2.3 MPa and pre-stress of 2.2 MPa. The measured harvested energy density on the load was 1 μJ/cm^3 at 300 Hz. Using Eq. (11), the theoretical harvested energy was determined to be 0.9 μJ/cm^3. In [54], Zucca et al. used a Terfenol-D rod with a dynamic load of 2.75 MPa and a pre-load stress peak of 4.55 MPa at 300 Hz. The harvested power on the load was approximately 80 mW and the harvested power estimated using Eq. (11) was 75 mW. In [53], Davino et al. used a Galfenol rod with a peak dynamic load of 15 MPa, preload stress of 16 MPa at 0.35 Hz, and R_{load} and R_{coil} values of 1 kΩ each. In that case, the harvested energy on the load was 4 μJ/cm^3, while the estimated value was 3.7 μJ/cm^3. These results show that the model can predict the harvested energy very well when the harvester is loaded with a resistance, with

only very small discrepancies that can be attributed to simplifying assumptions, e.g., negligible inductive effects. Therefore, the model and the associated energy density expression can be regarded as a reliable tool for estimation of the energy harvesting capability of the materials.

Additionally, Eq. (10) shows that the theoretical maximum power that can be harvested is not dependent on the mechanical structure, and is only dependent on the stress and magnetic field variations at the optimal frequency and the properties of the magnetostrictive material itself. This conclusion is in accordance with the conclusions in the literature [99].

From another perspective, the optimal frequency described in this section is defined using Eq. (12), which is derived in detail in the appendix:

$$\omega_0 = \frac{l_{ms}(R_{coil}+R_{load})}{\mu S N^2} \tag{12}$$

where S and N represent the cross-section and the number of turns of the coil, and l_{ms} represents the length of the sample. ω_0 is neither the mechanical nor the electrical natural frequency, but is an optimal frequency derived from the magnetic point of view. Based on the description of Eq. (12), the frequency is dependent on the coil structure and the smart material's permeability μ. In that case, a material with low permeability, e.g., Terfenol-D, would induce a higher ω_0 and a smaller coil would thus be required, while high magnetic permeability materials will make the structural design easier.

It should be noted that the negative impact of a high permeability may be regarded as a solely influence of the magnetoelectric energy conversion, where the dynamic magnetic field results from induced currents in the coil. In the proposed linearized model, the stress effect is a shifting of the BH curve. The energy will be the highest when both induction field and magnetic field are maximized. As the stress primarily acts on the induction field, the

excitation field will become the highest for lower permeability, inducing larger converted energy eventually.

4.4 Figure of merit for the self-induced magnetic field

The previous comparisons did not consider the bias mechanical excitation. As a final comparison to investigate the bias condition further, the ratio of the square of the magnetoelastic coefficient to the dynamic permeability $\frac{\theta^2}{\mu}$ was estimated using the developed model (Eq. (10)). The figures of merit of Terfenol-D and A Galfenol and the typical performances of the low magnetostriction materials are presented in figure 13 using a step size of 1 MPa.

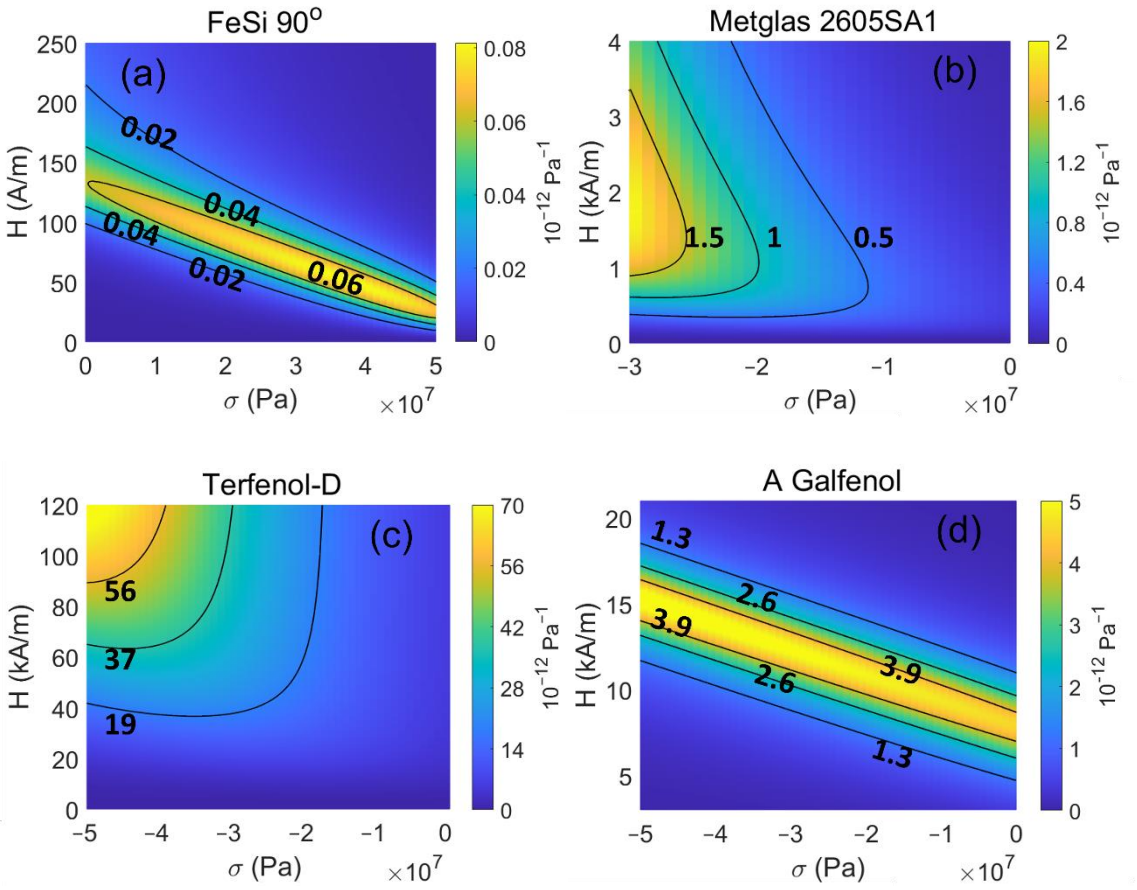

Figure 13 – Figure of merit $\frac{\theta^2}{\mu}$ for (a) FeSi 90°, (b) Metglas 2605SA1, (c) Terfenol-D, and (d) A Galfenol as a function of the bias mechanical stress and the bias magnetic field.

The results confirmed that the energy harvesting performance of Terfenol-D is not sensitive to the stress level or the magnetic field at low levels, and that higher magnetic fields and stress levels always provide a higher harvesting capability. In contrast, in the Galfenol case, the performance is highly sensitive to the bias condition, as shown in figure 13(b). Detailed information about the materials in the low and high magnetic field ranges is given in the next section.

V – Discussion

To provide a comprehensive and clear comparison of the different methods and conditions, the results estimated using the Ericsson cycle, $\frac{\Delta B}{\Delta \sigma}$, and $\left(\frac{\partial B}{\partial \sigma}\right)^2 / \mu$ are given under low and high magnetic fields in tables 6, 7 and 8.

Material	Compressive		Tensile	
	0–1 kA/m	0–150 kA/m	0–1 kA/m	0–15 kA/m
Terfenol-D	16	**57185**	-	-
AG Galfenol	226	**10663**	-	-
A Galfenol	12	**9558**	177	**478**
FeCo-2V	985	**4223**	557	**1125**
Metglas 2605SA1	517	**1204**	254	**478**
FeSi NO	330	**1066**	208	**316**
CGO	267	267	-	-
Nickel	-	-	43	**2200**
FeSi-90°	-	-	106	106
HGO	-	-	42.3	42.3
AC CoFeSiB	-	-	19	19
A CoFeSiB	-	-	29	29

Table 6. Energy density harvested (μJ/cm3) with the Ericsson cycle under different magnetic field ranges and stress levels. The bold values indicate the best performance for each material under tensile or compressive stresses.

Material	Compressive		Tensile	
	0–1 kA/m	1–150 kA/m	0–1 kA/m	1–15 kA/m
Terfenol-D	0.7 (1 kA/m)	**10** (45 kA/m)	-	-
AG Galfenol	10 (1 kA/m)	**20** (6 kA/m)	-	-
A Galfenol	0.5 (1 kA/m)	**20** (11.5 kA/m)	6 (1 kA/m)	**20** (6 kA/m)
FeCo-2V	**25** (750 A/m)	24 (1 kA/m)	**10** (150 A/m)	4 (1 kA/m)
Metglas 2605SA1	**20** (400 A/m)	16 (1 kA/m)	10 (119 A/m)	-
FeSi NO	**8.6** (750 A/m)	8.4 (1 kA/m)	**5.6** (275 A/m)	3 (1 kA/m)
CGO	**150** (60 A/m)	2 (1 kA/m)	-	-
Nickel	-	-	2 (1 kA/m)	**4** (4.4 kA/m)
FeSi-90°	-	-	18 (70 A/m)	-
HGO	-	-	10 (48 A/m)	-
AC CoFeSiB	-	-	1 (100 A/m)	-
A CoFeSiB	-	-	2.8 (48 A/m)	-

Table 7. Highest magnetoelastic coefficient (mT/MPa) values of the different materials under different magnetic field ranges and stress levels with a stress variation of 50 MPa. The corresponding bias magnetic field is given in brackets and the bold values represent the best performance for each material under tensile or compressive stresses.

Material	Compressive		Tensile	
	0–1 kA/m	1–150 kA/m	0–1 kA/m	1–15 kA/m
Terfenol-D	0.03 (−14 MPa, 1 kA/m)	**87.5** (−50 MPa, 150 kA/m)	-	-
AG Galfenol	5 (−2 MPa, 1 kA/m)	**12.8** (−50 MPa, 10 kA/m)	-	-
A Galfenol	0.04 (0 MPa, 1 kA/m)	**5.3** (−50 MPa, 15 kA/m)	0.4 (48 MPa, 0.6 kA/m)	**4.9** (19 MPa, 7.13 kA/m)
FeCo-2V	1.3 (−40 MPa, 1 kA/m)	**3.3** (−50 MPa, 3.35 kA/m)	**2.4** (0 MPa, 780 A/m)	2.4 (0 MPa, 1.4 kA/m)
Metglas 2605SA1	1.6 (−30 MPa, 1 kA/m)	**2.0** (−30 MPa, 1.7 kA/m)	**1** (0 MPa, 390 A/m)	0.5 (0 MPa, 1 kA/m)
FeSi NO	0.2 (−50 MPa, 1 kA/m)	**0.4** (−50 MPa, 2.2 kA/m)	**0.4** (0 MPa, 160 A/m)	0.006 (0 MPa, 1 kA/m)
CGO	**8.7** (−2 MPa, 0.04 kA/m)	0.9 (−10 MPa, 1 kA/m)	-	-
Nickel	-	-	0.04 (26 MPa, 1 kA/m)	**1.3** (50 MPa, 25 kA/m)
FeSi-90°	-	-	0.08 (37 MPa, 51 A/m)	-
HGO	-	-	0.009 (50 MPa, 96 A/m)	-
AC CoFeSiB	-	-	0.002 (50 MPa, 300 A/m)	-
A CoFeSiB	-	-	2.6 (0 MPa, 300 A/m)	-

Table 8. Highest $\left(\frac{\partial B}{\partial \sigma}\right)^2 / \mu$ (10−12 Pa−1) values of the different materials under different magnetic field ranges and stress levels with a stress variation of 1 MPa. The corresponding bias magnetic field is given in brackets and the bold values represent the best performance for each material under tensile or compressive stresses.

Table 6 indicates that in the ideal case when there is no magnetic field limitation, the materials with the highest magnetostriction, e.g., Terfenol-D and Galfenol, do have the highest energy densities. Under low magnetic fields, the order may be reversed. In addition to these two materials, the best material option may be FeCo-2V.

The magnetoelastic coefficients obtained with a higher stress level variation are given in table 7; this table provided more information about the optimum magnetic field. In the cases of nickel and FeCo-2V, their ultimate Ericsson cycles showed energy densities of the same order of magnitude, as indicated in table 6. Although the magnetoelastic coefficient of FeCo-2V shows an obvious peak (e.g., when compared with Nickel) as depicted in figure 10(b) that demonstrates the necessity of magnetic field optimization, the optimum magnetic field is presented in table 7. This table also shows that for materials such as FeCo-2V and Metglas 2605SA1, a higher magnetic field does not actually mean a higher magnetoelastic coefficient.

However, in realistic devices, the dynamic magnetic field results from induction in coils, and the energy density is dependent on the magnetic permeability. To investigate the effects of the bias mechanical excitation, the bias magnetic field, and the self-induced dynamic magnetic field, the $\left(\frac{\partial B}{\partial \sigma}\right)^2 / \mu$ coefficient values are presented in table 8. The optimum bias condition is given in each case. Interestingly, the giant magnetostrictive materials showed the highest values, because of their relatively small permeability values, as shown in table 7. The resulting energy density may be estimated, for example, by considering a dynamic stress level of 1 MPa, which leads to energy densities in the hundreds of μJ/cm^3 range for Terfenol-D, and tens of μJ/cm^3 range for Fe-Co and Metglas 2605SA1.

VI – Conclusion

This study compared ferromagnetic materials with low and high magnetostrictive characteristics for use in energy harvesting applications by considering them independently from any structural aspects and without considering air gap-induced reluctance changes. Correlations were established between energy density and magnetic indicators under various conditions. An anhysteretic model was developed to unify the operating conditions (stress, magnetic field), thus allowing fair comparison of the studied materials. The conclusions based on the different conditions and different methods are drawn as follows:

1. The ultimate energy density and the energy density in the low magnetic field range (0–1 kA/m) were estimated using Ericsson cycles. The results show good correlation between the magnetostriction and ultimate energy density properties. Under −50 MPa stress, Terfenol-D shows an ultimate energy density of approximately 60 mJ/cm^3, one decade greater than the other materials, but it requires a high field bias. In the low magnetic field range, FeCo-2V and Metglas 2605SA1 showed the highest energy densities of 985 $\mu J/cm^3$ and 515 $\mu J/cm^3$, respectively. Under 50 MPa stress, an energy density of 0.02–0.6 mJ/cm^3 was achieved for all materials in the low field range (1 kA/m). FeCo-2V achieved the highest value with more than 0.56 mJ/cm^3, while the highest energy density was achieved by nickel with 2.2 mJ/cm^3 at 15 kA/m. Iron-silicon alloys and CoFeSiB showed energy densities of the same order of magnitude (≈0.01–0.1 mJ/cm^3) for both low and high magnetic fields.
2. Assessment of the magnetoelastic coefficient demonstrated that materials with high magnetostriction no longer give the highest values under all conditions. Figures 10 and 11 showed the different performances of each material. In these figures, Terfenol-D showed a relatively small magnetoelastic coefficient (10 mT/MPa) under

an optimal bias field of 45 kA/m, particularly when compared with that of FeCo-2V. However, Terfenol-D reached a stable state above 20 kA/m, which means that harvesters featuring this material would not be sensitive to the magnetic field bias. In contrast, Galfenol is highly sensitive to the bias condition. In that case, the bias magnetic field must be controlled precisely in accordance with the stress level. Table 7, which gives the optimum bias magnetic fields, provides more detailed information for selection of the magnetic field bias.

3. Under realistic conditions in a compact device, magnets provide the magnetic bias excitation. An additional dynamic magnetic field contribution results from induced currents in surrounding coils by application of the dynamic stress. In this case, the harvesting process results in a small loop around the bias magnetic field and the stress level. The energy density can then be estimated directly using the figure of merit $\left(\frac{\partial B}{\partial \sigma}\right)^2/\mu$. This comparison shows that Terfenol-D gives the highest value of 87.5×10^{-12} Pa^{-1} under −50 MPa stress at 150 kA/m, while Galfenol gives the second highest value of 12.8×10^{-12} Pa^{-1}, also under −50 MPa stress, but with a much lower bias magnetic field of 10 kA/m. Apart from Terfenol-D and Galfenol, FeCo-2V and Metglas 2605SA1 show the highest harvesting capabilities with values of 3.3×10^{-12} Pa^{-1} and 2×10^{-12} Pa^{-1} with a bias magnetic field of less than 5 kA/m.

In summary, highly magnetostrictive materials such as Terfenol-D and Galfenol are used widely in energy harvesting. However, their cost and requirements for high bias fields raise questions over their implementation. Conversely, under low fields, materials with lower magnetostriction are just as competitive and much more cost-effective. However, because some of the materials under consideration have not been widely studied in the energy harvesting domain, there is a lack of information and relevant studies in the literature.

Therefore, the different methods devised in this study were verified using the few studies available, but systematically produced consistent results.

For the future investigation of the energy harvesting, this article could give a guidance for estimation of the energy density of an energy harvester with electrical circuit for actually harvesting the energy along with signal conditioning, potentially including nonlinear interfaces. With a fully developed structure, the stress-strain (T(S)) loop could also be a helpful tool for providing insights through a precise assessment of the levels of mechanical energy required for performing the energy harvesting process.

Data availability statement

All data that support the findings of this study are included within the article.

Conflict of interest

The authors declare that they have no known competing financial interests or personal relationships that could have appeared to influence the work reported in this paper.

Appendix. Calculation of energy density for self-induced magnetic fields

To convert mechanical energy into magnetic energy, it is necessary to have variations in both flux density *B* and magnetic field *H*. For the small-scale devices described in the literature, a permanent magnet applies the bias magnetic field. A coil surrounding the magnetostrictive material is subjected to an induced current that results from mechanical stress application. The coil may be connected to a resistive load, ensuring that the induced current is in phase with the electromotive force, and shifted by 90° with respect to B, resulting in an elliptical BH loop.

In the following calculation, it is assumed that the harvesting coil is connected to a load resistance and that the reluctance of all materials other than the magnetostrictive magnetic materials was neglected. For a closed magnetic circuit with a coil winding around the magnetostrictive material, we obtain:

$$H_{ms}l_{ms} = N_m I_{0m} - NI \quad (13)$$

H_{ms} and l_{ms} represent the magnetic field and the magnetostrictive sample length, and $N_m I_{0m}$ and NI represent the magnetomotive force (mmf) of the magnet and that of the coil, respectively, where N is the number of turns of the coil and I is the current. The mmf of the magnet is given by:

$$N_m I_{0m} = M_m e_m \quad (14)$$

where M_m and e_m are the magnetizing force and the thickness of the magnet, respectively. The magnetic behavior of the magnetostrictive material was then linearized in terms of both the magnetic field and the mechanical stress:

$$B_{ms} = \mu H_{ms} + \theta\sigma \quad (15)$$

where $\theta = \frac{\partial B}{\partial \sigma}$ and σ represents the magnetoelastic coefficient, which depends on the magnetic field and the mechanical stress; B_{ms} and μ represent the local linearized magnetic flux density and the permeability, respectively. The equivalent circuit schematic of the coil is shown in figure 14.

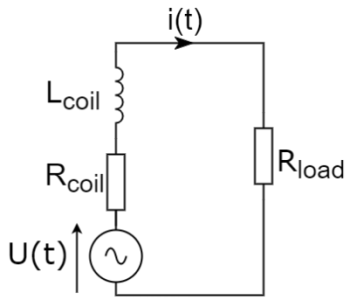

Figure 14 – Equivalent circuit schematic of the coil around the magnetostrictive sample.

In the electrical circuit, we obtain:

$$U(t) = (R_{coil} + R_{load} + jL_{coil}\omega) \times i(t) = N\frac{d\phi}{dt} \quad (16)$$

where ϕ is the magnetic flux. By combining $B = \frac{\phi}{S}$ with Eqs. (14), (15), and (16), Eq. (13) becomes:

$$\frac{\frac{\phi}{S} - \theta\sigma}{\mu} l_{ms} = M_m e_m - \frac{N^2 \frac{d\phi}{dt}}{R_{coil} + R_{load} + jL_{coil}\omega} \quad (17)$$

where S is the cross-section of the magnetostrictive material. We assumed only small variations around a bias value for the following variables:

$$\sigma = \sigma_0 e^{j\omega t}$$

$$\phi = \phi_0 + \phi_{dyn} e^{j\omega t}$$

$$B(t) = B_0 + B_{dyn} e^{j\omega t}$$

$$H(t) = H_0 + H_{dyn} e^{j\omega t}$$

Using Eq. (17), and by considering the varying terms with $e^{j\omega t}$ only, we obtain:

$$\frac{\frac{\phi_{dyn} e^{j\omega t}}{S} - \theta\sigma_0 e^{j\omega t}}{\mu} l_{ms} = -\frac{N^2}{R_{coil} + R_{load} + jL_{coil}\omega} j\omega\phi_{dyn} e^{j\omega t} \quad (18)$$

Equation (18) can then be simplified as:

$$\phi_{dyn} \times \left(1 + \frac{j\omega\mu S}{l_{ms}} \frac{N^2}{R_{coil} + R_{load} + jL_{coil}\omega}\right) = \theta\sigma_0 S \quad (19)$$

With $B = \frac{\phi}{S}$, and using Eq. (15), we can derive the variations in the magnetic flux density B and the magnetic field H as follows:

$$B_{dyn} = \frac{\theta\sigma_0}{1 + j\omega\frac{\mu S}{l_{ms}} \times \frac{N^2}{R_{coil} + R_{load} + jL_{coil}\omega}} \quad (20)$$

$$H_{dyn} = \frac{1}{\mu}\left(B_{dyn} - \theta\sigma_0\right) = \frac{\theta\sigma_0}{\mu}\left(\frac{1}{1 + j\omega\frac{\mu S}{l_{ms}} \times \frac{N^2}{R_{coil} + R_{load} + jL_{coil}\omega}} - 1\right) \quad (21)$$

Therefore, the converted power and its average value can be presented as follows:

$$P(t) = H(t)\frac{dB(t)}{dt}$$

$$< \mathrm{P(t)} >= \frac{1}{2}\mathrm{Re}\left\{\mathrm{H_{dyn}}\mathrm{e}^{\mathrm{j}\omega\mathrm{t}}\overline{\mathrm{j}\omega B_{dyn}\mathrm{e}^{\mathrm{j}\omega\mathrm{t}}}\right\} = \frac{\omega}{2}\mathrm{Re}\{-\mathrm{jH_{dyn}}\overline{B_{dyn}}\} \quad (22)$$

Using Eq. (22), the energy of a small cycle can be derived as:

$$\mathrm{W} = \mathrm{T} \times < \mathrm{P(t)} >= \frac{2\pi}{\omega} \times \frac{\omega}{2}\mathrm{Re}\left\{-\mathrm{jH_{dyn}}\overline{B_{dyn}}\right\} = \pi\mathrm{Re}\left\{-\mathrm{jH_{dyn}}\overline{B_{dyn}}\right\} \quad (23)$$

Under the assumption that $\mathrm{L}\omega \ll \mathrm{R_{coil}}$, and the reference angular velocity defined in Eq. (12) as:

$$\omega_0 = \frac{\mathrm{l_{ms}(R_{coil}+R_{load})}}{\mu \mathrm{SN}^2} \quad (12)$$

the variations in the magnetic flux density and the magnetic field can be simplified from Eqs. (20) and (21) as follows:

$$\mathrm{B_{dyn}} = \theta\sigma_0 \frac{1}{1+\mathrm{j}\frac{\omega}{\omega_0}} \quad (24)$$

$$\overline{\mathrm{B_{dyn}}} = \theta\sigma_0 \frac{1+\mathrm{j}\frac{\omega}{\omega_0}}{1+\left(\frac{\omega}{\omega_0}\right)^2} \quad (25)$$

$$\mathrm{H_{dyn}} = \frac{\theta\sigma_o}{\mu}\left(\frac{1}{1+j\frac{\omega}{\omega_o}} - 1\right) \quad (26)$$

Therefore, using Eqs. (25) and (26), Eq. (23) can be simplified as shown in Eq. (9):

$$\mathrm{W} = -\pi\frac{\theta^2\sigma_0^2}{\mu} \times \frac{\frac{\omega}{\omega_0}}{1+\left(\frac{\omega}{\omega_0}\right)^2} \quad (9)$$

Using Eq. (9), the maximum energy can be determined when $\frac{\omega}{\omega_0} = 1$, and the maximum energy is:

$$\mathrm{W_{max}} = -\pi\frac{\theta^2\sigma^2}{2\mu} \quad (10)$$

References

[1] Iannacci J 2019 Microsystem based energy harvesting (EH-MEMS): Powering pervasivity of the Internet of Things (IoT) – A review with focus on mechanical vibrations *J. King Saud Univ. Sci.* **31** 66–74. https://doi.org/10.1016/j.jksus.2017.05.019

[2] Ng I C L and Wakenshaw S Y L 2017 The Internet-of-Things: Review and research directions *Int. J. Res. Mark.* **34** 3–21. doi: 10.1016/j.ijresmar.2016.11.003.

[3] Marin-Garcia G, Vazquez-Guzman G, Sosa J M, Lopez A R, Martinez-Rodriguez P R and Langarica D 2020 Battery types and electrical models: A review *IEEE Int. Autumn Meeting on Power, Electronics and Computing*. doi: 10.1109/ropec50909.2020.9258711.

[4] Sanislav T, Mois G D, Zeadally S and Folea SC 2021 Energy harvesting techniques for Internet of Things (IoT) *IEEE Access* **9** 39530–39549. doi: 10.1109/access.2021.3064066.

[5] Shaikh F K and Zeadally S 2016 Energy harvesting in wireless sensor networks: A comprehensive review *Renew. Sustain. Energy Rev.* **55** 1041–1054. doi: 10.1016/j.rser.2015.11.010.

[6] Penella M T and Gasulla M. 2007 A review of commercial energy harvesters for autonomous sensors *IEEE Instrumentation & Measurement Technol. Conf*. doi: 10.1109/imtc.2007.379234.

[7] Bahl S, Nagar H, Singh I and Sehgal S 2020 Smart materials types, properties and applications: A review *Mater. Today: Proc.* **28** 1302–1306. doi: 10.1016/j.matpr.2020.04.505.

[8] Kök M, Qader I N, Dağdelen F and Aydoğdu Y. 2019 "Akıllı malzemeler üzerine derleme: Araştırmalar ve uygulamaları," *El-Cezeri Fen ve Mühendislik Dergisi* **6** 755–788. doi: 10.31202/ecjse.562177.

[9] Guyomar D and Lallart M 2011 Recent progress in piezoelectric conversion and energy harvesting using nonlinear electronic interfaces and issues in small scale implementation *Micromachines* **2** 274–294. doi: 10.3390/mi2020274.

[10] An L *et al.*, 2023 Energy harvesting using a magnetostrictive transducer based on switching control *Sens. Actuator. A: Phys.* **355** 114303. doi: 10.1016/j.sna.2023.114303.

[11] Kishore R and Priya S 2018 A review on low-grade thermal energy harvesting: Materials, methods and devices *Materials* **11** 1433. doi: 10.3390/ma11081433.

[12] Hao D *et al.* 2022 Solar energy harvesting technologies for PV self-powered applications: A comprehensive review *Renew. Energy* **188** 678–697. doi: 10.1016/j.renene.2022.02.066.

[13] Ahmad F F, Ghenai C and Bettayeb M 2021 Maximum power point tracking and photovoltaic energy harvesting for Internet of Things: A comprehensive review *Sustain. Energy Technol. Assess.* **47** 101430. doi: 10.1016/j.seta.2021.101430.

[14] Safaei M, Sodano H A and Anton S R 2019 A review of energy harvesting using piezoelectric materials: State-of-the-art a decade later (2008-2018). *Smart Mater. Struct.* **28** 113001. https://doi.org/10.1088/1361-665X/ab36e4

[15] Hathaway K B and Clark A E 1993 Magnetostrictive materials *MRS Bulletin* **18** 34–41. doi: 10.1557/s0883769400037337.

[16] Engdahl G 2000 *Handbook of Giant Magnetostrictive Materials* (Cambridge, MA: Academic Press). doi: 10.1016/b978-0-12-238640-4.x5014-1.

[17] Siang J, Lim M H and Salman Leong M 2018 Review of vibration-based energy harvesting technology: Mechanism and architectural approach *Int. J. Energy Res.* **42** 1866–1893. https://doi.org/10.1002/er.3986

[18] Ylli K, Hoffmann D, Willmann A, Becker P, Folkmer B and Manoli Y 2015 Energy harvesting from human motion: Exploiting swing and shock excitations *Smart Mater. Struct.* **24** 025029. doi: 10.1088/0964-1726/24/2/025029.

[19] Sundriyal P and Bhattacharya S 2018 Energy harvesting techniques for powering wireless sensor networks in aircraft applications: A review. *Sensors for Automotive and Aerospace Applications* pp. 55–76. doi: 10.1007/978-981-13-3290-6_4.

[20] Hosseinkhani A, Younesian S, Eghbali P, Moayedizadeh A and Fassih A 2021 Sound and vibration energy harvesting for railway applications: A review on linear and nonlinear techniques *Energy Rep* **7** 852–874. doi: 10.1016/j.egyr.2021.01.087.

[21] Ghodsi M, Ziaiefar H, Mohammadzaheri M and Al-Yahmedi A 2019 Development of magnetostrictive harvester for unmanned aerial vehicles (UAV) *1st Int. Conf. on Unmanned Vehicle Systems-Oman*. doi: 10.1109/uvs.2019.8658277.

[22] Li T and Lee P S 2022 Piezoelectric energy harvesting technology: From materials, structures, to applications *Small Struct.* **3** 2100128. https://doi.org/10.1002/sstr.202100128

[23] Uchino K. 2018 Piezoelectric energy harvesting systems—Essentials to successful developments. *Energy Technol.* **6** 829–848. https://doi.org/10.1002/ente.201700785

[24] Joule J P 1847 XVII. On the effects of magnetism upon the dimensions of iron and steel bars *The London, Edinburgh, and Dublin Philosophical Magazine and Journal of Science* **30** 76–87. doi: 10.1080/14786444708645656.

[25] Apicella V, Clemente C S, Davino D, Leone D and Visone C 2019 Review of modeling and control of magnetostrictive actuators *Actuators* **8** 45. doi: 10.3390/act8020045.

[26] Villari E 1865 Ueber die Aenderungen des magnetischen Moments, welche der Zug und das Hindurchleiten eines galvanischen Stroms in einem Stabe von Stahl oder Eisen hervorbringen *Annalen der Physik und Chemie* **202** 87–122. doi: 10.1002/andp.18652020906.

[27] Elhajjar R, Law C T and Pegoretti A 2018 Magnetostrictive polymer composites: Recent advances in materials, structures and properties *Prog. Mater. Sci.* **97** 204–229. https://doi.org/10.1016/j.pmatsci.2018.02.005

[28] Deng Z and Dapino M J 2018 Review of magnetostrictive materials for structural vibration control *Smart Mater. Struct.* **27** 113001. https://doi.org/10.1088/1361-665X/aadff5

[29] Gao C, Zeng Z, Peng S and Shuai C 2022 Magnetostrictive alloys: Promising materials for biomedical applications *Bioact. Mater.* **8** 177–195. https://doi.org/10.1016/j.bioactmat.2021.06.025

[30] Fang Z-W, Zhang Y-W, Li X, Ding H and Chen L-Q 2017 Integration of a nonlinear energy sink and a giant magnetostrictive energy harvester *J. Sound Vib.* **391** 35–49. doi: 10.1016/j.jsv.2016.12.019.

[31] Dai X, Wen Y, Li P, Yang J and Li M 2011 Energy harvesting from mechanical vibrations using multiple magnetostrictive/piezoelectric composite transducers *Sens. Actuator. A: Phys.* **166** 94–101. https://doi.org/10.1016/j.sna.2010.12.025

[32] Liu H, Cao C, Sun X, Zhao L and Cong 2020 Magnetostrictive iron-gallium alloy harvester with efficient two-mode AC-DC converting technology for effective vibration energy harvesting. *AIP Adv.* **10** 115304. https://doi.org/10.1063/5.0025550

[33] Mohanty A, Parida S, Behera R K and Roy T 2019 Vibration energy harvesting: A review *J. Adv. Dielectr*. **9** 1930001. doi: 10.1142/s2010135x19300019.

[34] Clemente C S, Mahgoub A, Davino D and Visone C 2017 Multiphysics circuit of a magnetostrictive energy harvesting device. *J. Intell. Mater. Syst. Struct*. **28** 2317–2330. https://doi.org/10.1177/1045389X16685444

[35] Zucca M, Bottauscio O, Beatrice C, Hadadian A, Fiorillo F and Martino L 2014 A study on energy harvesting by amorphous strips *IEEE Trans. Magn*. **50** 1–4. doi: 10.1109/tmag.2014.2327169.

[36] Deng Z, Scheidler J J, Asnani V M and Dapino M J 2016 Quasi-static major and minor strain-stress loops in textured polycrystalline $Fe_{81.6}Ga_{18.4}$Galfenol *J. Appl. Phys*. **120** 243901. doi: 10.1063/1.4972479.

[37] Park Y-W, Kang H-S and Wereley N M 2014 Conceptual design of rotary magnetostrictive energy harvester *J. Appl. Phys*. **115** 17E713. doi: 10.1063/1.4865976.

[38] Ueno T 2019 Magnetostrictive vibrational power generator for battery-free IoT application *AIP Adv.* **9** 035018. doi: 10.1063/1.5079882.

[39] *https://www.aone-alloy.com/supplier-177873-magnetostrictive-material*.

[40] Backman G, Lawton B and Morley N A 2019 Magnetostrictive energy harvesting: Materials and design study *IEEE Trans. Magn*. **55** 1–6. doi: 10.1109/tmag.2019.2891118.

[41] Deng Z and Dapino M J 2017 Review of magnetostrictive vibration energy harvesters *Smart Mater. Struct*. **26** 103001. doi: 10.1088/1361-665x/aa8347.

[42] Staley M E and Flatau A B 2005 Characterization of energy harvesting potential of Terfenol-D and Galfenol *Proc. SPIE* **5764**. doi: 10.1117/12.604871.

[43] Zhao X and Lord D G 2006 Application of the Villari effect to electric power harvesting *J. Appl. Phys*. **99** 08M703. doi: 10.1063/1.2165133.

[44] Wang L and Yuan F G 2008 Vibration energy harvesting by magnetostrictive material *Smart Mater. Struct*. **17** 045009. doi: 10.1088/0964-1726/17/4/045009.

[45] Tsutsumi E, del Rosario Z and Lee C 2012 Vibration energy harvesting using the nonlinear oscillations of a magnetostrictive material *Proc. SPIE* **8341** 834104. doi: 10.1117/12.914412.

[46] Liu L, Guo X and Lee C 2021 Promoting smart cities into the 5G era with multi-field Internet of Things (IoT) applications powered with advanced mechanical energy harvesters *Nano Energy* **88** 106304. doi: 10.1016/j.nanoen.2021.106304.

[47] Narita F and Fox M 2017 A review on piezoelectric, magnetostrictive, and magnetoelectric materials and device technologies for energy harvesting applications *Adv. Eng. Mater*. **20** 1700743. doi: 10.1002/adem.201700743.

[48] Lin C-h and Lin Y Z 2021. Analysis of nonlinear piezomagnetism for magnetostrictive terfenol-D composites. *J. Magn. Magn. Mater.* **540** 168490. https://doi.org/10.1016/j.jmmm.2021.168490

[49] Wun-Fogle M, Restorff J B, Leung K and Clark A E 1999 Magnetostriction of Terfenol-D heat treated under compressive stress. *Digests of the Intermag Conf.* **3** 3817–3819. https://doi.org/10.1109/intmag.1999.838000

[50] Ueno T 2016 U-shape magnetostrictive vibration based power generator for universal use *Proc. SPIE* **9806** 98060E. doi: 10.1117/12.2218759.

[51] Yan B, Zhang C and Li L 2015 Design and fabrication of a high-efficiency magnetostrictive energy harvester for high-impact vibration systems *IEEE Trans. Magn*. **51** (11) 1–4. doi: 10.1109/tmag.2015.2441295.

[52] Deng Z and Dapino M J 2015 Multiphysics modeling and design of galfenol-based unimorph harvesters *Proc SPIE* **9433** 94330B. doi: 10.1117/12.2085550.

[53] Davino D, Giustiniani A, Visone C and Adly A A 2012 Energy harvesting tests with galfenol at variable magneto-mechanical conditions *IEEE Trans. Magn*. **48** 3096–3099. doi: 10.1109/tmag.2012.2200036.

[54] Zucca M, Hadadian A and Bottauscio O 2015 Quantities affecting the behavior of vibrational magnetostrictive transducers *IEEE Trans. Magn*. **51** (1) 1–4. doi: 10.1109/tmag.2014.2359248.

[55] Hu J, Xu F, Huang A Q and Yuan F G 2010 Optimal design of a vibration-based energy harvester using magnetostrictive material (MsM) *Smart Mater. Struct.* **20** 015021. doi: 10.1088/0964-1726/20/1/015021.

[56] Ghodsi M, Ziaiefar H, Mohammadzaheri M and Al-Yahmedi A 2019 Modeling and characterization of permendur cantilever beam for energy harvesting *Energy* **176** 561–569. doi: 10.1016/j.energy.2019.04.019.

[57] Yamaura S, Nakajima T, Kamata Y, Sasaki T and Sekiguchi T 2020 Production of vibration energy harvester with impact-sliding structure using magnetostrictive Fe-Co-V alloy rod *J. Magn. Magn. Mater*. **514** 167260. doi: 10.1016/j.jmmm.2020.167260.

[58] Jen S U, Liu C C, Lin H R and Chou S H 2014 Frequency dependence of the magnetostrictive phenomenon in Metglas® 2605SA1 ribbon: A minor-loop case *AIP Adv*. **4** 127140. 10.1063/1.4905264.

[59] Deng Z and Dapino M J 2017 Magnetic flux biasing of magnetostrictive sensors *Smart Mater. Struct.* **26** 055027. doi: 10.1088/1361-665x/aa688b.

[60] Ito M, Kamada K, Yoshikawa A, Kawamata T, Fujieda S, Suzuki S, Minamitani T and Ueno T 2018 Shape-controlled crystal growth of Fe-Ga alloys to apply a magnetostrictive vibration energy harvester. *J. Alloys Compd.* **731** 898–902. https://doi.org/10.1016/j.jallcom.2017.10.109

[61] Taheri P, Barua R, Hsu J, Zamanpour M, Chen Y and Harris V G 2016 Structure, magnetism, and magnetostrictive properties of mechanically alloyed Fe81Ga19 *J Alloys Compd.* **661** 306–311. doi: 10.1016/j.jallcom.2015.11.037.

[62] Xu Y, Bader S and Oelmann B 2018. A survey on variable reluctance energy harvesters in low-speed rotating applications. *IEEE Sens. J.* **18** 3426–3435. https://doi.org/10.1109/JSEN.2018.2808377

[63] Yang Z, Nakajima K, Onodera R, Tayama T, Chiba D and Narita F 2018 Magnetostrictive clad steel plates for high-performance vibration energy harvesting *Appl. Phys. Lett.* **112** 073902. https://doi.org/10.1063/1.5016197

[64] Kurita H, Lohmuller P, Laheurte P, Nakajima K and Narita F 2022 Additive manufacturing and energy-harvesting performance of honeycomb-structured magnetostrictive Fe52–Co48 alloys. *Addit. Manuf.* **54** 102741. doi:10.1016/j.addma.2022.102741.

[65] Xia Z, Kang Y and Wang Q 2008 Developments in the production of grain-oriented electrical steel *J. Magn. Magn. Mater*. **320** 3229–3233. doi: 10.1016/j.jmmm.2008.07.003.

[66] Zhu L, Yoon H-S, Cho H-J, Um D-J and Koh C-S 2016 Finite-element analysis of magnetostriction force in power transformer based on the measurement of anisotropic magnetostriction of highly grain-oriented electrical steel sheet *IEEE Trans. Magn*. **52** (3) 1–4. doi: 10.1109/tmag.2015.2481466.

[67] Leuning N, Steentjes S, Schulte M, Bleck W and Hameyer K 2016 Effect of elastic and plastic tensile mechanical loading on the magnetic properties of NGO electrical steel *J. Magn. Magn. Mater*. **417** 42–48. doi: 10.1016/j.jmmm.2016.05.049.

[68] Permiakov V, Dupre L, Makaveev D and Melkebeek J 2002 Dependence of power losses on tensile stress for Fe–Si nonoriented steel up to destruction *J. Appl. Phys*. **91** 7854. doi: 10.1063/1.1446117.

[69] Agarwal D C 2004 Nickel and nickel alloys *Handbook of Advanced Materials: Enabling New Designs* (Hoboken NJ: Wiley) pp. 217–270. doi: 10.1002/0471465186.ch7.

[70] He J, Zhou L, Zhao D L and Wang X L 2009 Hysteresis loop shift behavior of CoFeSiB amorphous ribbons *J. Mater. Res*. **24** 1607–1610. doi: 10.1557/jmr.2009.0185.

[71] Pirota K, Kraus L, Chiriac H and Knobel M 2000 Magnetic properties and giant magnetoimpedance in a CoFeSiB glass-covered microwire *J. Magn. Magn. Mater*. **221** L243–L247. doi: 10.1016/s0304-8853(00)00554-0.

[72] Kraus L, Knobel M, Kane S N and Chiriac H 1999 Influence of Joule heating on magnetostriction and giant magnetoimpedance effect in a glass covered CoFeSiB microwire *J. Appl. Phys* **85** 5435–5437. doi: 10.1063/1.369967.

[73] *http://tdvib.com/galfenol/*.

[74] *http://tdvib.com/terfenol-d/*.

[75] Mahmoud R 2014 Mesure et modélisation du comportement magnéto-mécanique dissipatif des matériaux ferromagnétiques à haute limite élastique sous chargement multiaxial *PhD Thesis* École normale supérieure de Cachan-ENS Cachan.

[76] Berbyuk V 2013 Vibration energy harvesting using Galfenol-based transducer *Proc. SPIE* **8688** 86881F. doi: 10.1117/12.2009812.

[77] Rizzo K-J, Hubert O and Daniel L 2010 Magnetic and magnetostrictive behavior of iron-silicon single crystals under uniaxial stress *IEEE Trans. Magn*. **46** (2), 270–273. doi: 10.1109/tmag.2009.2032146.

[78] Agayan V 1996 Thermodynamic model of ideal magnetostriction *Physica Scripta* **54** 514–521. doi: 10.1088/0031-8949/54/5/011.

[79] Chiriac H, Neagu M, Vazquez M and Hristoforou E 2002 Saturation magnetostriction measurement in nearly zero magnetostrictive Co-rich glass-covered amorphous wires *J. Magn. Magn. Mater*. **242–245** 251–253. doi: 10.1016/s0304-8853(01)01246-x.

[80] Qiu F, Ren W, Tian G Y, Gao Y and Gao B 2015 *IEEE Far East NDT New Technology & Application Forum* The effect of stress on the domain wall behavior of high permeability grain-oriented electrical steel. doi: 10.1109/fendt.2015.7398341.

[81] Raghunathan A, Klimczyk P and Melikhov Y 2013 Application of Jiles-Atherton model to stress induced magnetic two-phase hysteresis *IEEE Trans. Magn*. **49** (7), 3187–3190. doi: 10.1109/tmag.2013.2243823.

[82] Liu Y, Ducharne B, Sebald G, Makihara K and Lallart M 2023 Investigation of energy harvesting capabilities of Metglas 2605SA1 *Appl. Sci*. **13** 3477. doi: 10.3390/app13063477.

[83] Jia Z, Liu W, Zhang Y, Wang F and Guo D 2006 A nonlinear magnetomechanical coupling model of giant magnetostrictive thin films at low magnetic fields. *Sens. Actuator. A: Phys*. **128** 158–164. https://doi.org/10.1016/j.sna.2006.01.018

[84] Birss R 1971 Magnetomechanical effects in the Rayleigh region *IEEE Trans. Magn.* **7** 113–133. doi: 10.1109/TMAG.1971.1067015.

[85] Shi P 2021 One-dimensional magneto-mechanical model for anhysteretic magnetization and magnetostriction in ferromagnetic materials. *J. Magn. Magn. Mater.* **537** 168212. https://doi.org/10.1016/j.jmmm.2021.168212

[86] Adly A, Davino D, Giustiniani A and Visone C 2010 Experimental tests of a magnetostrictive energy harvesting device toward its modeling. *J. Appl. Phys*. **107** 09A935. doi: 10.1063/1.3357403.

[87] Lewis-Beck M, Bryman A and Futing Liao T. 2012. Coefficient of determination. *The SAGE Encyclopedia of Social Science Research Methods* (Thousand Oaks, CA: Sage) p 2. https://doi.org/10.4135/9781412950589.n132

[88] Thanh Tung N, Taxil G, Nguyen H H, Ducharne B, Lallart M, Lefeuvre E, Kuwano H and Sebald G. 2022 Ultimate electromechanical energy conversion performance and energy storage capacity of ferroelectric materials under high excitation levels *Appl. Energy* **326** 119984. https://doi.org/10.1016/j.apenergy.2022.119984

[89] Lallart M, Cottinet P J, Guyomar D and Lebrun L 2012. Electrostrictive polymers for mechanical energy harvesting. *J. Polym. Sci. B: Polym. Phys.* **50** 523–535. https://doi.org/10.1002/polb.23045

[90] Zhang B, Ducharne B, Gupta B, Sebald G, Guyomar D and Gao J 2017 Experimental sea wave energy extractor based on piezoelectric Ericsson cycles *J. Intell. Mater. Syst. Struct*. **29** 1102–1112. doi: 10.1177/1045389x17730917.

[91] Sebald G, Pruvost S and Guyomar D 2007 Energy harvesting based on Ericsson pyroelectric cycles in a relaxor ferroelectric ceramic *Smart Mater. Struct*. **17** 015012. doi: 10.1088/0964-1726/17/01/015012.

[92] Ducharne B, Zurek S, Daniel L, and Sebald G 2022 An anisotropic vector hysteresis model of ferromagnetic behavior under alternating and rotational magnetic field *J. Magn. Magn. Mater*. **549** 169045. doi: 10.1016/j.jmmm.2022.169045.

[93] Chwastek K R, Baghel A P S, De Campos M F, Kulkarni S V and Szczyglowski J 2015 A description for the anisotropy of magnetic properties of grain-oriented steels. *IEEE Trans. Magn*. **51** (12) 3–7. https://doi.org/10.1109/TMAG.2015.2449775

[94] Dapino M J, Smith R C and Flatau A B 2000 Structural magnetic strain model for magnetostrictive transducers *IEEE Trans. Magn*. **36** (3) 545–556. doi: 10.1109/20.846217.

[95] Li P, Wen Y, Liu P, Li X and Jia C 2010 A magnetoelectric energy harvester and management circuit for wireless sensor network *Sens. Actuator. A: Phys*. **157** 100–106. doi: 10.1016/j.sna.2009.11.007.

[96] Seuaciuc-Osório T and Daqaq M F 2008 Effect of bias conditions on the optimal energy harvesting using magnetostrictive materials *Proc. SPIE* **6928** 69280B. https://doi.org/10.1117/12.779624

[97] Staley M E 2005 Development of a prototype magnetostrictive energy harvesting device *MSc Thesis* University of Maryland, College Park

[98] Moffett M B, Clark A E, Wun-Fogle M, Linberg J, Teter J P and McLaughlin E A 1991 Characterization of Terfenol-D for magnetostrictive transducers *J. Acoust. Soc. Am.* **89** 1448–1455. https://doi.org/10.1121/1.400678

[99] Badel A, Formosa F and Lallart M 2015 Electromechanical transducers. *Micro Energy Harvesting* (Weinheim: Wiley-VCH) pp 27–60. https://doi.org/10.1002/9783527672943.ch3